Published as Ayscue et al. Inorg. Chem. 2021, 60, 9727–9744. https://doi.org/10.1021/acs.inorgchem.1c01025

Structure-Property Relationships in Photoluminescent Bismuth Halide Organic Hybrid Materials

R. Lee Ayscue,[†] Valérie Vallet,[‡] Jeffery A. Bertke,[†] Florent Réal, [‡,*] and Karah E. Knope[†,*]

† Department of Chemistry, Georgetown University, 3700 O Street, NW, Washington, D.C. 20057, USA (kek44@georgetown.edu)

‡ Univ. Lille, CNRS, UMR 8523−PhLAM−Physique des Lasers Atomes et Molécules, 59000 Lille, France (florent.real@univ-lille.fr)

Supporting Information

Contents

Synthesis of Bi-Halide-Organic Hybrid Materials

Compound **1**, $[Bi_2Cl_6(terpy)_2][Bi_2Cl_6(terpy)_2]\bullet H_2O$.

$BiCl_3$ (0.0315g, 0.1mmol) and terpyridine (0.0234g, 0.1mmol) were added into 2mL of methanol and 1mL of H_2O in a two-dram glass vial. A white solid immediately precipitated upon mixing. The pH of the solution was 2-3. The sample was left for 48 hours on the benchtop under ambient conditions, after which a microcrystalline solid along with colorless block single crystals were obtained. The product was allowed to dry in air after washing with water and methanol. Yield (based on corresponding Bi content): 98.4%. Elemental analysis: Calc. (Obs.): C, 32.31 (32.50); N, 7.54 (7.61); H, 2.17 (2.23). It is worth noting that **1** was also observed in the presence of TC, absent pH adjustment as described below. Additionally, washing the sample with acetone or acetonitrile results in the loss of lattice water and phase conversion to previously reported $Bi_2C_6l(terpy_2)$.[1]

Compound **2, [**$Bi_2Cl_4(terpy)_2(k_2\text{-}TC)_2$]

$BiCl_3$ (0.0315g, 0.1mmol) was added to 1.8mL of methanol and sonicated for 5 min. A separate ligand solution was prepared consisting of terpyridine (0.0234g, 0.1mmol), thiophene monocarboxylic acid (TCA) (0.0128g, 0.1mmol), 0.2mL of 1M KOH in methanol, and 1mL of methanol. These mixtures were then combined in a 2-dram vial, with a total reaction volume of 3 mL. The reaction solution immediately became turbid upon combination of the reactants and a white solid precipitate with no appreciable luminescence was observed. After stirring or sonicating for less than 1 minute, a color change from the white precipitate to a faint yellow solid with considerable yellow-green luminescence under a 356 nm handlamp was noted. Continued stirring or sonication for 5 minutes yielded the luminescent phase. The final reaction pH was 5-6. The bulk reaction product was isolated, washed with methanol, and allowed to dry in air. To obtain single crystals of **2** suitable for structure determination, the same general protocol was followed; however, the reaction was left undisturbed for 24 hours. Colorless blocks crystals were isolated. Yield (based on corresponding Bi content) = 76.4%. Elemental analysis: Calc. (Obs.): C, 37.52(37.36); N, 6.56 (6.47); H, 2.20 (2.14).

Compound **3A-Cl**, $[BiCl(terpy)(k_2\text{-}TC)_2]$

For bulk sample, $BiCl_3$ (0.0315g, 0.1mmol) was combined with 0.1mL 5M HNO_3 and 1.1mL of methanol. This sonicated until full solubility was obtained. A separate ligand solution was prepared consisting of terpyridine (0.0234g, 0.1mmol), thiophene monocarboxylic acid (TCA) (0.0385g, 0.3mmol), 0.8mL of 1M KOH, and 1mL of methanol. Both mixtures were then combined for a total reaction solution of 3mL into a 2-dram vial. Immediately upon combination, a cloudy white solid precipitate formed with no appreciable luminescence. For bulk sample preparation, the combined reaction solution was stirred. Upon stirring less than 1 minute, the predominant phase became faint yellow with intense yellow-green luminescence under a 356 nm handlamp. Stirring was maintained for a total time of 5 minutes, and the final reaction pH was 5-6. Unfortunately, this bulk sample also contained microcrystalline white precipitants indexed as KCl and KNO_3 via PXRD (Figure S28). While water washes were able to remove the majority of KCl and KNO_3, a

phase pure product could not be achieved. Attempts to fully remove this unwanted byproduct through variation of reaction conditions/methods, further post-synthetic washings, or attempted phase separations proved unsuccessful and would often lead to coprecipitation of undesired Bi phases or degradation of desired product. Nitric acid additions were needed to ensure $BiCl_3$ solubility and thwart BiOCl impurities that otherwise plagued this system and act as a potential interferent in luminescent studies. For preparations without nitric acid addition, exhausted attempts to remove BiOCl through various washing and separation techniques also proved unsuccessful, and therefore necessitating HNO_3 addition. Alternative acids were also explored but did not result in a phase pure product. Thus, minor phase impurities of KCl or KNO_3 are acknowledged in bulk sample of **3-Cl**, and therefore precluded subsequent elemental analysis and accurate yield determination. For single crystal preparation of **3-Cl**, the reaction solution described above was left undisturbed for 24 hours, in which clusters of elongated spear-like crystals form that possess significant yellow luminescence. These crystals were manually separated and used for diffraction and other reported characterization including luminescent studies. Furthermore, no observable difference in luminescent behavior was observed as compared to bulk sample with acknowledge impurities.

Compound **3A-Br**, [BiBr(terpy)(k_2-TC)$_2$]

Bulk sample of **3-Br** was synthesized by mixing $BiBr_3$ (0.0450mg, 0.1mmol), terpyridine (0.0235g, 0.1mmol), and TCA (0.0387g, 0.3mmol) in 2.8mL of H_2O and 0.2mL of 1M KOH. Uniform yellow crystalline product formed overnight. This product was filtered, washed with water and MeOH, and dried in air. Yield was obtained at 71.7% based on corresponding Bi content. Elemental analysis: Calc. (Obs.): C, 38.67 (38.41); N, 5.41 (5.28); H, 2.21 (2.14).

Compound **3B-Cl**, [BiCl(terpy)(k_2-TC)$_2$]

3B-Cl was obtained under the same reaction conditions as **3A-Cl**, apart from extending reaction time, resulting is an isostructural polymorph of **3A-Cl**. Notably, phase **3B-Cl** exhibited marginally greener luminescence than **3A-Cl** under 356 nm handlamps illumination. Bulk sample were prepared via stirring for the 24-hour duration; however, aforementioned BiOCl or KCl/KNO_3 impurities were also obtained. These phase impurities, identified by PXRD, precluded subsequent elemental analysis. Single crystals of **3B-Cl** were prepared under the same reaction conditions; however, combined mixtures were left on the benchtop and not agitated for 48 hours yielding small single crystalline blocks of the desired phase. These crystals were manually separated from the bulk for phase determination and comparative luminescence studies similar to those described for **3A-Cl**.

Compound **4**, [BiCl(terpy)(k_2-TC)$_2$][Bi(terpy)(k_2-TC)$_3$]•(TCA)

Bulk crystalline material of **4** was prepared by mixing $BiCl_3$ (0.0315g, 0.1mmol), terpyridine (0.0234g, 0.1mmol), thiophene monocarboxylic acid (TCA) (0.0385g, 0.3mmol), 2.8mL of H_2O and 0.2mL of 1M KOH into a two-dram vial at a reaction pH of 4-5. Upon rest on the benchtop, faint green block crystals with uniform green luminescence were obtained, washed with water, air dried and manually separated for further characterization. Yield based on Bi content was found to be 78.6%; Elemental analysis: Calc. (Obs.): C, 42.40 (42.17); N, 7.97 (7.86); H, 3.56 (3.48).

Compound **5**, **[**$BiBr_3$(terpy)(MeOH)][$BiBr_3$(terpy)(MeOH)]

Bulk sample of **5** was synthesized by mixing $BiBr_3$ (0.0450mg, 0.1mmol) and terpyridine (0.0235g, 0.1mmol) in 3.0mL of MeOH. Yellow crystalline blocks formed overnight and were filtered, washed with fresh MeOH, and dried in air. In some preparation TC (0.0387g, 0.3mmol) was also added; however, no TC coordination was observed and **5** was still obtained without pH adjustment. Product yield based on Bi content was determined to be 91.3%; Elemental analysis: Calc. (Obs.): C, 26.91 (27.12); N, 5.89 (5.96); H, 2.12 (2.19).

Compound **6**, [$BiBr_2$(terpy)(k_2-TC)][BiBr(terpy)(k_2-TC)$_2$]

Yellow crystalline product of **6** was obtained by additions of $BiBr_3$ (0.0450mg, 0.1mmol), terpyridine (0.0235g, 0.1mmol), and TCA (0.0387g, 0.3mmol) in 2.8mL of MeOH and 0.2mL of 1M KOH in MeOH. This reaction solution was capped and heated to 50°C in a dry heating block overnight. Solid yellow crystals were observed, filtered, washed with fresh MeOH, and dried in air. Notably, 6 and **3A-Br** were received as mixed products without heating and were difficult to discern by morphology, color, or emissive color. Product yield based on Bi content was determined to be 82.8%; Elemental analysis: Calc. (Obs.): C, 35.44 (35.17); N, 5.61 (5.50); H, 2.05 (1.96).

3A-$Bi_{1-x}Eu_xCl$, [$Bi_{1-x}Eu_x$Cl(terpy)(k_2-TC)$_2$] (x = 0.001, 0.005, 0.01, 0.05)

Mixed heterometallic Bi/Eu reactions, **3A-$Bi_{1-x}Eu_xCl$**, followed the same synthetic procedure as the homometallic Bi preparations of **3A-Cl** described above with the exception of varied additions of 0.1M $EuCl_3$ solutions. This exchange for Bi and Eu starting materials was made to maintain the same total quantity of metal(Bi/Eu) incorporated. Total reaction volume was maintained at 3mL with corresponding decreases in methanol with increasing volumes of 0.1M $EuCl_3$ solution. The varied additions are summarized below:

Sample	Addition of $BiCl_3$ solid	Addition of 0.1M $EuCl_3$ hydrate and corresponding amount	Synthetic Eu doping percentage
3-$Bi_{0.999}Eu_{0.001}Cl$	0.0314g / 0.0999µmol	10µL / 0.0001µmol	0.1%
3-$Bi_{0.995}Eu_{0.005}Cl$	0.0313g / 0.0995µmol	50µL / 0.0005µmol	0.5%
3-$Bi_{0.99}Eu_{0.01}Cl$	0.0311g / 0.099µmol	100µL / 0.001µmol	1.0%
3-$Bi_{0.95}Eu_{0.05}Cl$	0.0300g / 0.095µmol	500µL / 0.005µmol	5.0%

As in the homometallic **3A-Cl** phase, trace KCl and KNO_3 impurities persisted in these compounds inhibiting accurate elemental analysis and definitive yield calculations. Manually separated single crystals were used for data reported herein. However, no influence on luminescence behavior was observed between comparison of separated single crystals and bulk sample with acknowledged impurity. Attempts to dope beyond 5% Eu led to unwanted phase separation.

Eu-1, $[Eu_2(terpy)_2(k_2\text{-}TC)_4(\mu\text{-}TC)_2(H_2O)_2]\bullet 0.43H_2O$,

While **Eu-1** was prepared and reported previously under hydrothermal conditions by Batrice and colleagues,[2] this compound also forms as a synthetic analog to conditions used for **3-Cl**, upon substituting molar equivalents of $BiCl_3$ for $EuCl_3\bullet 6H_2O$. Therefore, **Eu-1** was selected for comparative structural and luminescence analysis to **3A-Cl** and the **3A-Bi$_{1-x}$Eu$_x$Cl** series.

Crystallographic Refinement Details

General Info

Unit cells were identified using APEX3. Several frame series, including a fast scan to account for potential topped reflection intensities, were integrated and filtered for statistical outliers using SAINT then corrected for absorption by integration using SAINT/SADABS v2014/2 to sort, merge, and scale the combined data.[3] The structure was phased by intrinsic or direct methods and assigned an unambiguous space group for each model.[4] The space group choice was confirmed by successful convergence of the full matrix least-squares refinement on F^2. Further model refinement was then completed using SHELXE software.[5] Reported structural parameters such as bond lengths, interaction angles, and centroid distances were compiled using PLATON.[6] Across this series of crystal system P-1. Cif's for all homo systems were deposited and can be found in the Cambridge Structural Data Centre under the reference numbers 2063326-2063333.

1

A structural model consisting of two halves of the target dimer and one lattice water molecule per asymmetric unit was developed from a single indexed cell refinement. This model converged with $wR_2 = 0.0420$ and $R_1 = 0.0276$ for 412 parameters with 2 restraints against 5540 [$F_o > 4sig(F_o)$] data. The water H atoms were located in the difference map. The O-H distances were restrained to be 0.88 (0.01 Å). Remaining H atoms were included as riding idealized contributors. Water H atoms were assigned as 1.5 times U_{eq} of the carrier atom; remaining H atom displacement parameters were assigned as 1.2 times carrier U_{eq}.

2

Phase indexed to a single cell domain, this structural model consists of one half of the target dimer per asymmetric unit was developed. This model converged with $wR_2 = 0.0484$ and $R_1 = 0.0342$ for 299 parameters with 161 restraints against 3157 [$F_o > 4sig(F_o)$] data. The thiophene ring is disordered over two orientations. The like S-C and C-C distances were restrained to be similar (esd 0.01 Å). The C24/C24B atom pair was constrained to have equal x,y,z positions and equal anisotropic displacement parameters. Similar displacement amplitudes (esd 0.01 Å) were imposed on disordered sites overlapping by less than the sum of van der Waals radii. H atoms positions were calculated and assigned displacement parameters as 1.2 times carrier U_{eq}.

3A-Cl

A structural model of the target complex was developed from the refinement of a single crystal cell. This model converged with $wR_2 = 0.0757$ and $R_1 = 0.0384$ for 471 parameters with 1153 restraints against 4415 [$F_o > 4sig(F_o)$] data. The thiophene ligand in the same plane as the terpy is disordered over two orientations. The like S-C, O-C, and C-C distances were restrained to be similar (esd 0.01 Å). The C25/C25B atom pair was constrained to have equal x,y,z positions as

well as equal anisotropic displacement parameters due to overlapping positions across disorder. The other two ligand species coordinated to the Bi metal center are substitutionally disordered Cl/thiophene groups. The Bi-Cl distances were restrained to be similar (esd 0.01 Å). The like S-C, O-C, and C-C distances of the thiophene ligand were restrained to be similar (esd 0.01 Å) as well. Rigid-bond restraints were imposed on displacement parameters for all sites and similar displacement amplitudes (esd 0.01 Å) were imposed on disordered sites overlapping by less than the sum of van der Waals radii. H atoms were included as riding idealized contributors and were assigned displacement parameters as 1.2 times the carrier atom's U_{eq}. Likely due to small unresolvable twinning, three disagreeable reflections were omitted from the final refinement.

3A-Br

A structural model of the target complex was developed and converged with $wR_2 = 0.1025$ and $R_1 = 0.0394$ for 471 parameters with 1104 restraints against 4764 [$F_o > 4sig(F_o)$] data. The thiophene ligand in the same plane as the terpy is disordered over two orientations. The like S-C, O-C, and C-C distances were restrained to be similar (esd 0.01 Å). The C25/C25B atom pair was constrained to have equal x,y,z positions as well as equal anisotropic displacement parameters. The other two species coordinated to the Bi metal center are positionally disordered Br/thiophene groups. The Bi-Br distances were restrained to be similar (esd 0.01 Å). The like S-C, O-C, and C-C distances of the thiophene ligand were restrained to be similar (esd 0.01 Å) as well. Rigid-bond restraints were imposed on displacement parameters for all sites and similar displacement amplitudes (esd 0.01 Å) were imposed on disordered sites overlapping by less than the sum of van der Waals radii. H atoms were included as riding idealized contributors. H atom displacement parameters were assigned as 1.2 times carrier U_{eq}. Four disagreeable reflections, like due to a small, twinned domain that could not be indexed, was omitted from the final refinement.

3B-Cl

A structural model consisting of the target molecule was developed from a single indexed unit cell. This model converged with $wR_2 = 0.0262$ and $R_1 = 0.0102$ for 417 parameters with 466 restraints against 4328 [$F_o > 4sig(F_o)$] data. The thiophene portion of both TC ligands are disordered over two orientations. The like S-C and C-C distances were restrained to be similar (esd 0.01 Å). Rigid-bond restraints were imposed on displacement parameters for all disordered sites, and similar displacement amplitudes (esd 0.01 Å) were imposed on disordered sites overlapping by less than the sum of van der Waals radii. H atoms were included as riding idealized contributors and were assigned displacement parameters 1.2 times its carrier atom U_{eq}. The (0 1 1) reflection was omitted from the final refinement because it was partially obscured by the shadow of the beam stop.

4

A structural model consisting of two Bi complexes and a disordered and half-occupied thiophene monocarboxylic acid molecules per asymmetric unit. This model converged with $wR_2 = 0.0721$ and $R_1 = 0.0337$ for 1033 parameters with 1410 restraints against 11549 [$F_o > 4sig(F_o)$] data. The ring portion of all of the coordinated TC ligands are all disordered over two orientations along free rotation of C#4 and C#5 bonds. The like S-C and C-C distances were restrained to be similar (esd 0.01 Å). The partially occupied TCA molecule in the outer coordination sphere is positionally disordered about a symmetry site. The like S-C, O-C, and C-C distances were restrained to be similar (esd 0.01 Å). The atoms were also restrained to behave relatively isotropic. Similar displacement amplitudes (esd 0.01 Å) were imposed on disordered sites overlapping by less than

the sum of van der Waals radii. Several disordered atom pairs (C#4 and C#4B) were constrained to have equal x,y,z positions and anisotropic displacement parameters. Hydroxyl H atom positions, R-OH, were optimized by rotation about R-O bonds with idealized O-H and R--H distances. Remaining H atoms were included as riding idealized contributors. Hydroxyl H atom U's were assigned as 1.5 times U_{eq} of the carrier atoms, while remaining H atom displacement parameters were assigned as 1.2 times carrier U_{eq}. Three reflections were omitted from the final refinement because they were partially obscured by the shadow of the beam stop.

5

A structural model consisting of two of the target complexes was developed from a single indexed cell domain. This model converged with $wR_2 = 0.0351$ and $R_1 = 0.0219$ for 441 parameters with 6 restraints against 6894 [$F_o > 4\text{sig}(F_o)$] data. Atom C11 was restrained to be more isotropic. The hydroxyl H atoms were located in the difference map, and their positions were allowed to refine. Remaining H atoms were included as riding idealized contributors. Hydroxyl H atom displacement parameters were assigned as 1.5 times U_{eq} of the carrier atoms, while remaining H atom displacement parameters were assigned as 1.2 times carrier U_{eq}.

6

Based on a single indexed cell domain, the refined model consists of two unique monomers in the asymmetric unit. This model converged with $wR_2 = 0.0385$ and $R_1 = 0.0238$ for 726 parameters with 1425 restraints against 7009 [$F_o > 4\text{sig}(F_o)$] data. The first complex consists of one Bi metal center, one terpy ligand, one TC ligand, and two bromides. The thiophene ring of the TC is disordered over two positions through free rotation of C24-C25 bond. The like S-C and C-C distances were restrained to be similar (esd 0.01 Å). The second complex consists one Bi metal center, one terpy ligand, one full occupancy bromide, and two substitutionally disordered TC/Br ligands. Three-part disorder is present at one of the TC/Br sites, which is a summation of TC rotational disorder and substitutional disorder with Br. Like S-C, C-C, and C-O distances of the positionally disordered TC were restrained to be similar (esd 0.01 Å). Rigid-bond restraints were imposed on displacement parameters for all sites, and similar displacement amplitudes (esd 0.01 Å) were imposed on disordered sites overlapping by less than the sum of van der Waals radii. Select atoms were restrained to be more isotropic to resolve slight divergence in displacement parameters. H atoms were included as riding idealized contributors. H atom displacement parameters were assigned as 1.2 times carrier U_{eq}.

Thermal Ellipsoid Plots

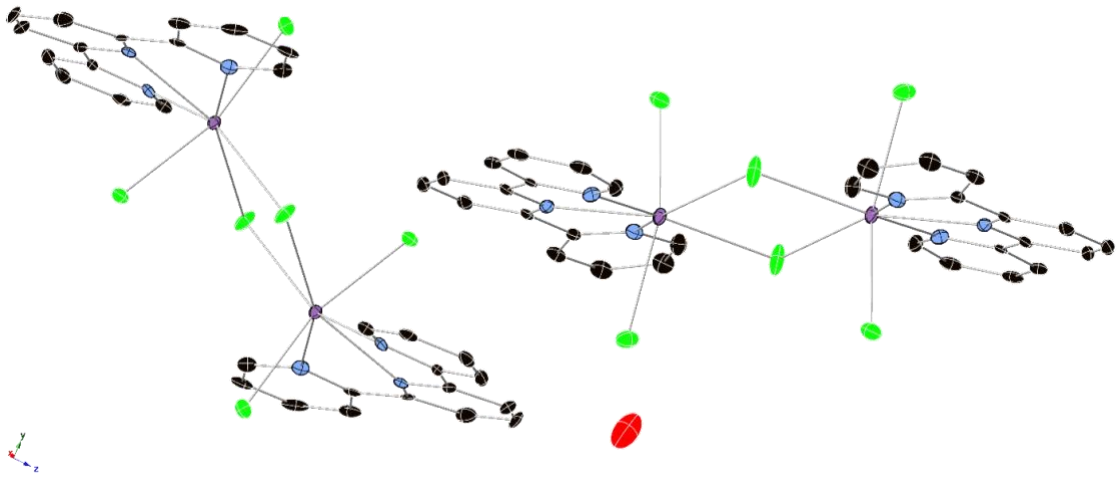

Figure S1. Thermal ellipsoid plot of dimeric unit of **1**, shown at 50% probability. Color code: Bi, purple; Cl, green; O, red; N, blue; C, black. H was not shown for clarity.

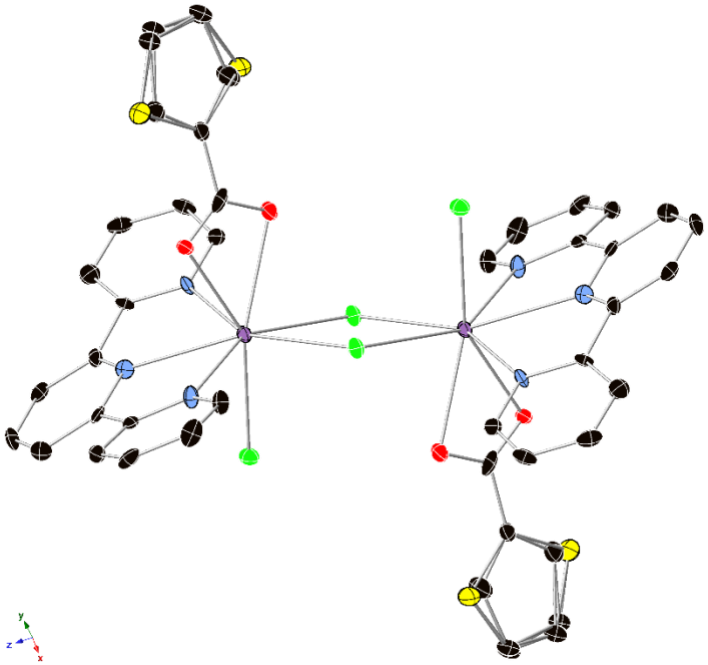

Figure S2. Thermal ellipsoid plot of dimeric unit of **2**, shown at 50% probability. Color code: Bi, purple; Cl, green; S, yellow; O, red; N, blue; C, black. H was not shown for clarity.

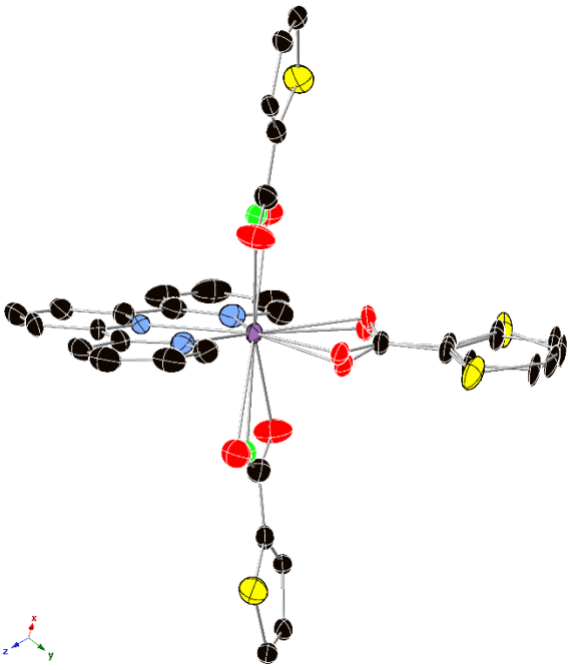

Figure S3. Thermal ellipsoid plot of dimeric unit of **3A-Cl**, shown at 50% probability. Color code: Bi, purple; Cl, green; S, yellow; O, red; N, blue; C, black. H was not shown for clarity.

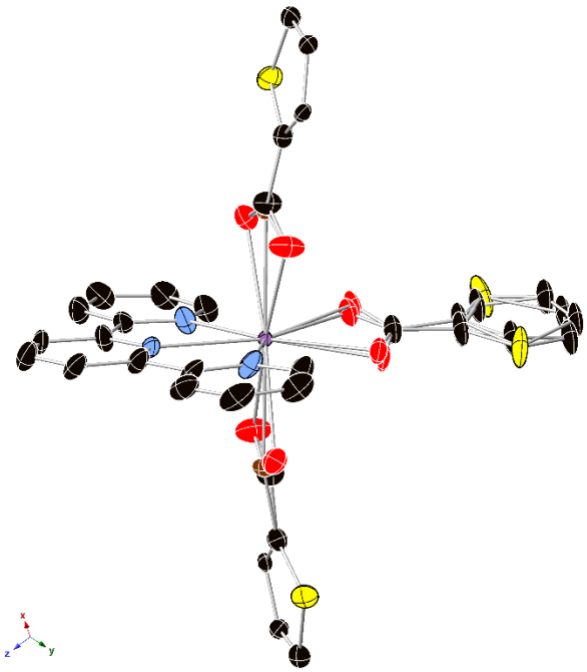

Figure S4. Thermal ellipsoid plot of dimeric unit of **3A-Br**, shown at 50% probability. Color code: Bi, purple; Br, brown; S, yellow; O, red; N, blue; C, black. H was not shown for clarity.

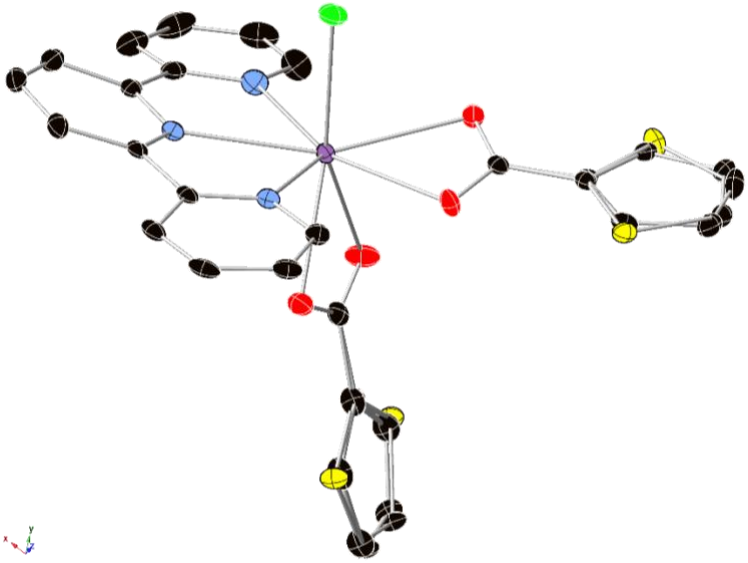

Figure S5. Thermal ellipsoid plot of dimeric unit of **3B-Cl**, shown at 50% probability. Color code: Bi, purple; Cl, green; S, yellow; O, red; N, blue; C, black. H was not shown for clarity.

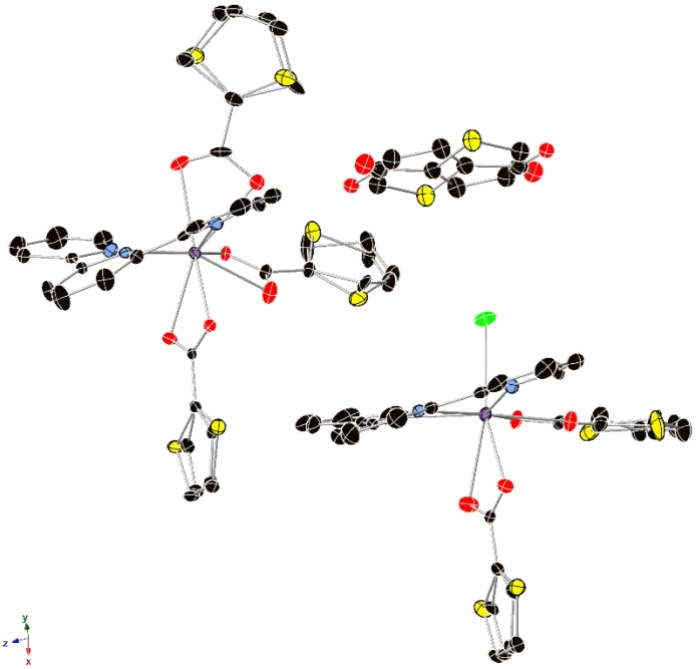

Figure S6. Thermal ellipsoid plot of dimeric unit of **4**, shown at 50% probability. Color code: Bi, purple; Cl, green; S, yellow; O, red; N, blue; C, black; H, hydrogen. Hydrogens were only shown for protonation and charge neutrality of TC and ride occupancy of bound . Other hydrogens were not shown for clarity.

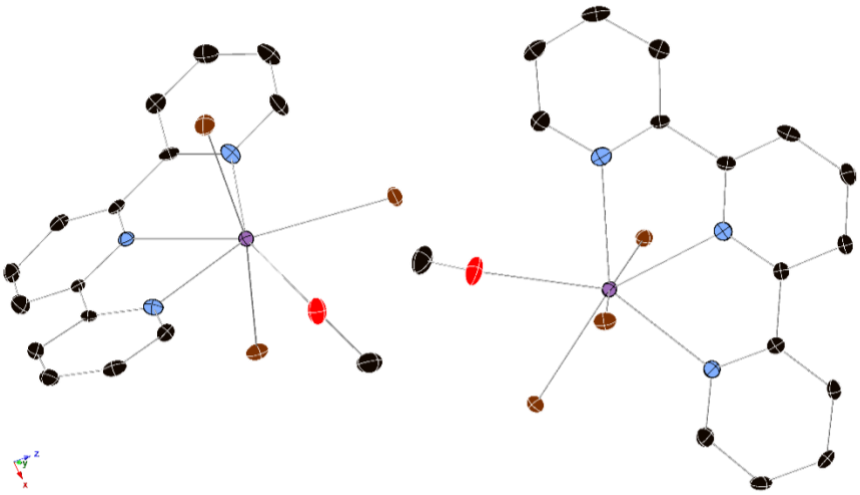

Figure S7. Thermal ellipsoid plot of dimeric unit of **5**, shown at 50% probability. Color code: Bi, purple; Br, brown; S, yellow; O, red; N, blue; C, black. H was not shown for clarity.

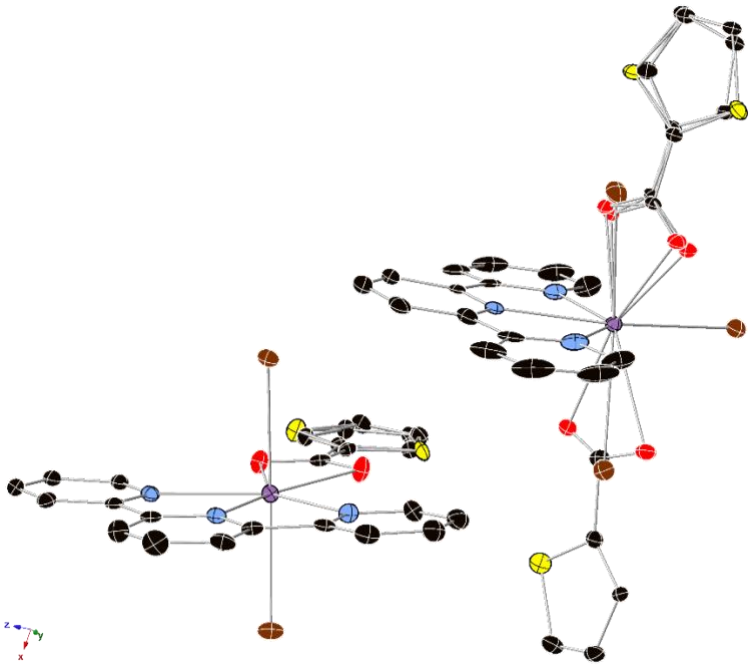

Figure S8. Thermal ellipsoid plot of dimeric unit of **6**, shown at 50% probability. Color code: Bi, purple; Br, brown; S, yellow; O, red; N, blue; C, black. H was not shown for clarity.

Relevant Bond Distances

Table S1. Metal-ligand bond distances for compounds **1** and **2**.

1		**2**	
Bi(1)-Cl(1)	2.853(5) Å	Bi(1)-Cl(1)	2.7047(1) Å
Bi(1)-Cl(2)	2.650(5) Å	Bi(1)-Cl(2)	2.8554(2) Å
Bi(1)-Cl(3)	2.716(5) Å	Bi(1)-Cl(1)#3	2.8655(2) Å
Bi(1)-Cl(1)#1	3.019(5) Å	Bi(1)-O(21)	2.4485(1) Å
Bi(1)-N(1)	2.445(4) Å	Bi(1)-O(22)	2.5338(1) Å
Bi(1)-N(2)	2.457(4) Å	Bi(1)-N(1)	2.5940(1) Å
Bi(1)-N(3)	2.526(4) Å	Bi(1)-N(2)	2.5249(1) Å
Bi(1)-Bi(1)#1	4.594(8) Å	Bi(1)-N(3)	2.5058(1) Å
		Bi(1)-Bi(1)#3	4.4404(2) Å
Bi(2)-Cl(4)	2.795(5) Å		
Bi(2)-Cl(5)	2.643(5) Å		
Bi(2)-Cl(6)	2.717(5) Å		
Bi(2)-Cl(4)#2	3.002(5) Å		
Bi(1)-N(4)	2.442(4) Å		
Bi(1)-N(5)	2.459(4) Å		
Bi(1)-N(6)	2.618(5) Å		
Bi(2)-Bi(2)#2	4.695(8) Å		

Symmetry Transformation used to generate equivalent atoms:
#1 = 1-x,1-y,-z
#2 = -x,2-y,1-z
#3 = 1-x, -y, -z

Table S2. Metal-ligand bond distances for compounds **3A-Cl**, **3A-Br**, and **3B-Cl**.

3A-Cl		**3A-Br**		**3B-Cl**	
Bi(1)-Cl(1B)	2.5879(1) Å	Bi(1)-Br(1B)	2.7953(1) Å	Bi(1)-Cl(1)	2.6228(1) Å
Bi(1)-Cl(1)	2.5889(1) Å	Bi(1)-Br(1)	2.7935(1) Å	Bi(1)-O(21)	2.3857(1) Å
Bi(1)-O(21)	2.5310(1) Å	Bi(1)-O(21)	2.5431(1) Å	Bi(1)-O(22)	2.6022(1) Å
Bi(1)-O(22)	2.4350(1) Å	Bi(1)-O(22)	2.4200(1) Å	Bi(1)-O(31)	2.5094(1) Å
Bi(1)-O(21B)	2.4368(1) Å	Bi(1)-O(21B)	2.4218(1) Å	Bi(1)-O(32)	2.6700(1) Å
Bi(1)-O(22B)	2.5278(1) Å	Bi(1)-O(22B)	2.5424(1) Å	Bi(1)-N(1)	2.4394(1) Å
Bi(1)-O(31)	2.6787(1) Å	Bi(1)-O(31)	2.6077(1) Å	Bi(1)-N(2)	2.5381(1) Å
Bi(1)-O(32)	2.6013(1) Å	Bi(1)-O(32)	2.5380(1) Å	Bi(1)-N(3)	2.6101(1) Å
Bi(1)-O(31B)	2.6700(1) Å	Bi(1)-O(31B)	2.6137(1) Å		
Bi(1)-O(32B)	2.5997(1) Å	Bi(1)-O(32B)	2.5368(1) Å		
Bi(1)-N(1)	2.4944(1) Å	Bi(1)-N(1)	2.4913(1) Å		
Bi(1)-N(2)	2.5245(1) Å	Bi(1)-N(2)	2.5255(1) Å		
Bi(1)-N(3)	2.4919(1) Å	Bi(1)-N(3)	2.4962(1) Å		

Table S3. Metal-ligand bond distances for **4**, **5**, and **6**.

4		**5**		**6**	
Bi(1)-O(21)	2.4790(2) Å	Bi(1)-Br(1)	2.9054(2) Å	Bi(1)-Br(1)	2.7954(2) Å
Bi(1)-O(22)	2.5292(2) Å	Bi(1)-Br(2)	2.7742(2) Å	Bi(1)-Br(2)	2.8501(2) Å
Bi(1)-O(31)	2.5351(2) Å	Bi(1)-Br(3)	2.8812(2) Å	Bi(1)-O(21)	2.4859(2) Å
Bi(1)-O(32)	2.4643(2) Å	Bi(1)-O(41)	2.6280(2) Å	Bi(1)-O(22)	2.5276(2) Å
Bi(1)-O(41)	2.5308(2) Å	Bi(1)-N(1)	2.6061(2) Å	Bi(1)-N(1)	2.4565(2) Å
Bi(1)-O(42)	2.5970(2) Å	Bi(1)-N(2)	2.5122(2) Å	Bi(1)-N(2)	2.4961(2) Å
Bi(1)-N(1)	2.5960(2) Å	Bi(1)-N(3)	2.4723(2) Å	Bi(1)-N(3)	2.5292(2) Å
Bi(1)-N(2)	2.5183(2) Å				
Bi(1)-N(3)	2.5156(2) Å	Bi(2)-Br(4)	2.9491(2) Å	Bi(2)-Br(3)	2.9871(2) Å
		Bi(2)-Br(5)	2.7610(2) Å	Bi(2)-Br(4)	2.8144(2) Å
Bi(2)-Cl(1)	2.6514(2) Å	Bi(2)-Br(6)	2.8535(2) Å	Bi(2)-Br(5)	2.9757(2) Å
Bi(2)-O(71)	2.4623(2) Å	Bi(2)-O(51)	2.6474(2) Å	Bi(2)-O(51)	2.3928(2) Å
Bi(2)-O(72)	2.5742(2) Å	Bi(2)-N(4)	2.4994(2) Å	Bi(2)-O(52)	2.6477(2) Å
Bi(2)-O(81)	2.4856(2) Å	Bi(2)-N(5)	2.4887(2) Å	Bi(2)-O(51B)	2.2301(2) Å
Bi(2)-O(82)	2.5573(2) Å	Bi(2)-N(6)	2.5724(2) Å	Bi(2)-O(52B)	2.5727(2) Å
Bi(2)-N(21)	2.4899(2) Å			Bi(2)-O(61)	2.4506(2) Å
Bi(2)-N(22)	2.4971(2) Å			Bi(2)-O(62)	2.7380(2) Å
Bi(2)-N(23)	2.5306(2) Å			Bi(2)-N(4)	2.4453(2) Å
				Bi(2)-N(5)	2.4845(2) Å
				Bi(2)-N(6)	2.5053(2) Å

Table S4. Terpyridine Ligand Torsion Angles for **3A-Cl** and **3B-Cl**.

	3A-Cl (°)	**3B-Cl** (°)
$C_4C_5C_6C_7$	1.37(1)	-13.58(1)
$C_9C_{10}C_{11}C_{12}$	2.13(1)	15.79(1)
$N_1C_5C_6N_2$	2.16(1)	-13.23(1)
$N_2C_{10}C_{11}N_3$	1.45(1)	14.46(1)

Intermolecular Packing Diagrams

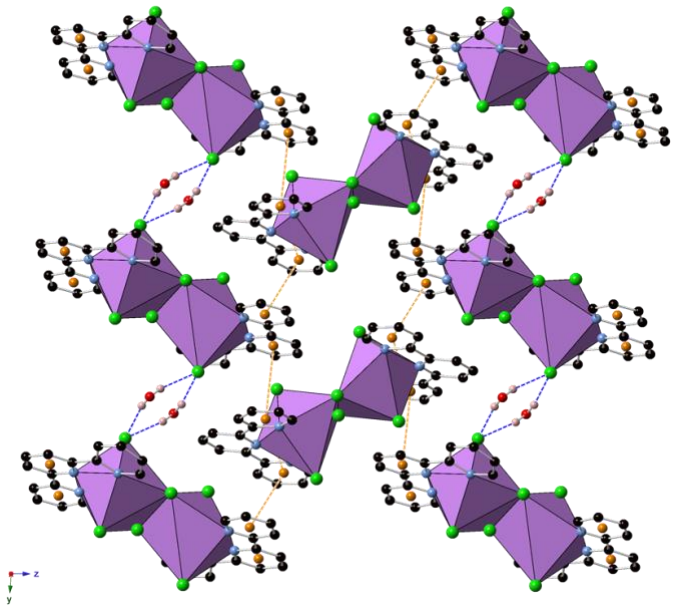

Figure S9. Packing diagram of **1** exhibiting supramolecular interactions. Green, blue, black, red, and pink spheres correspond to chloride, nitrogen, oxygen, and hydrogen atoms, respectively. Hydrogen atoms of terpy ligands are excluded for clarity. Purple polyhedra represent local coordination environment of Bi metal center. Ring centroid positions and stacking interactions are shown as orange spheres and dashed lines. Hydrogen bonding interactions between outer coordination sphere water and chloride atoms are shown as blue dashed lines. Overall, 3D supramolecular connectivity through π-π stacking interactions, is displayed as orange dashed lines between centroid positions.

Figure S10. Packing diagram of **2** exhibiting supramolecular interactions. Green, yellow, blue, black, red, and pink spheres correspond to chloride, sulfur, nitrogen, oxygen, and hydrogen atoms, respectively. Hydrogen atoms are excluded for clarity. Purple polyhedra represent local coordination environment of Bi metal center. Ring centroid positions and stacking interactions are shown as orange spheres and dashed lines. Overall, 2D supramolecular sheets through π-π stacking interactions, is displayed as orange dashed lines between centroid positions.

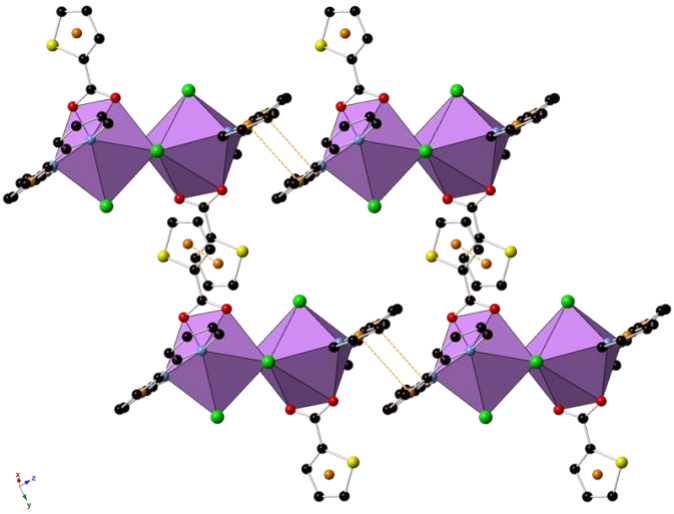

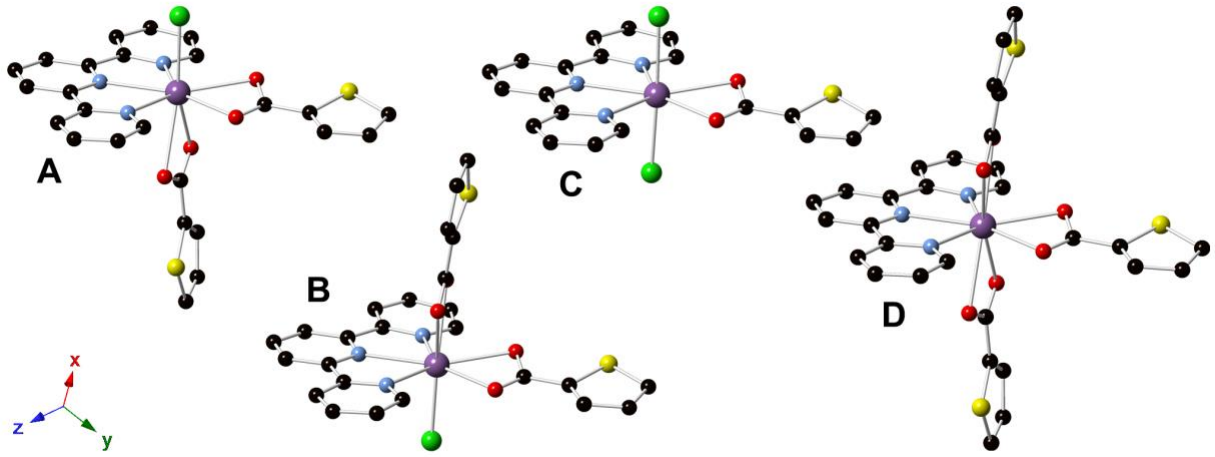

Figure S11: Illustration of all possible iteration Compound **3A-Cl** based substitutional disorder observed in SCXRD data. All structures are possible but are averaged in the overall crystal structure. The structure shown in A possess highest occupancy (**3A-Cl(a)** 1Cl and 1TC group), while B shows slightly lower occupancy with alternating coordination (**3A-Cl(b)** 1TC and 1Cl). Another way to consider this disorder is through the averaging of structures shown in C and D as well. Structure C (**3A-Cl(c)** 2 Cl occupancy) and D (**3A-Cl(d)** 2 TC occupancy) must occur in a co-crystallized alternating sequence within the single crystal lattice to avoid overlapping TC ligand positions. **3A-Br** also exhibits this disorder with structures designated as **3A-Br(a-d)**, respectively.

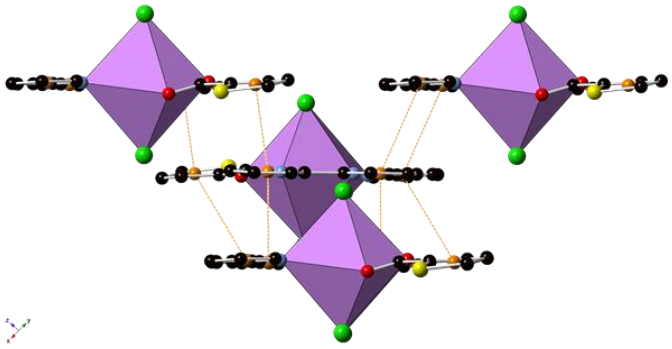

Figure S12. Packing diagrams for **3A-Cl(c)** with polyhedra representing Bi1 coordination spheres. Red, yellow, blue, black, and orange spheres represent oxygen, sulfur, nitrogen, carbon, and centroid positions, respectively. All terpy-terpy and terpy-TC π-π stacking interactions are illustrated as orange dashed lines and construct a 3D supramolecular structure. **3A-Br(c)** is isomorphous.

Figure S13. Packing diagrams for **3B-Cl** with polyhedra representing Bi1 coordination spheres. Red, yellow, blue, black, and orange spheres represent oxygen, sulfur, nitrogen, carbon, and centroid positions, respectively. Various terpy-terpy and terpy-TC π-π stacking interactions are illustrated as orange dashed lines. Overall, these extensive interactions construct a 3D supramolecular network.

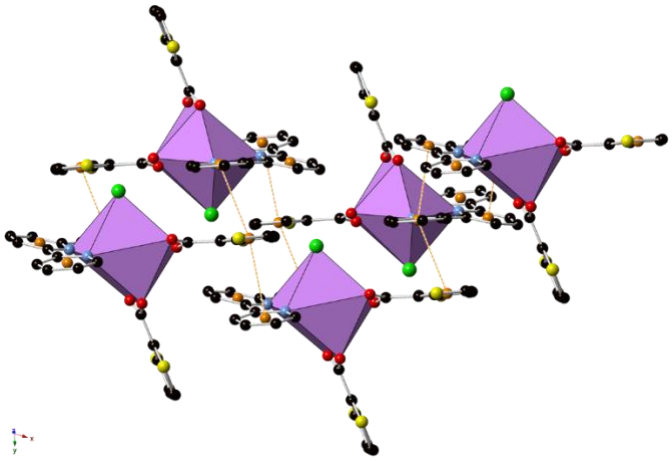

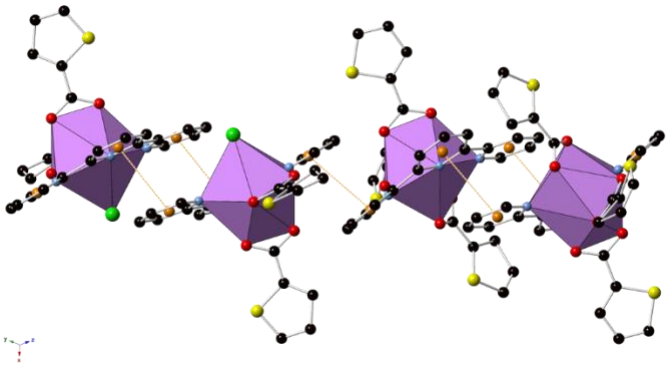

Figure S14. Supramolecular packing diagram of compound **4**. Purple polyhedra display local coordination environment of Bi metal center. Outer coordination sphere TCA unit was excluded for clarity of the packing diagram. Ring centroid positions and stacking events are shown as orange spheres and dashed lines. Overall, these stacking interactions form a 1D supramolecular chain.

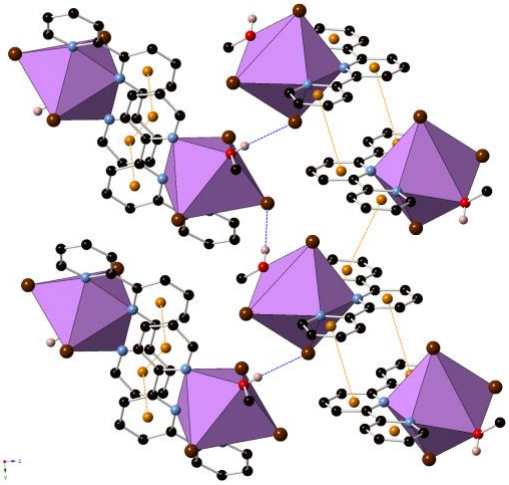

Figure S15. Packing diagram of **5** displays purple polyhedra for local coordination environment of Bi metal center. Brown, blue, black, and red spheres correspond to bromide, nitrogen, and oxygen atoms, respectively. Rendered as blue dashed lines, intermolecular hydrogen bonding is observed between methanol OH and adjacent bromides. Orange spheres and dashed lines are used to show centroid positions and π-π stacking interactions for specified terpy rings.

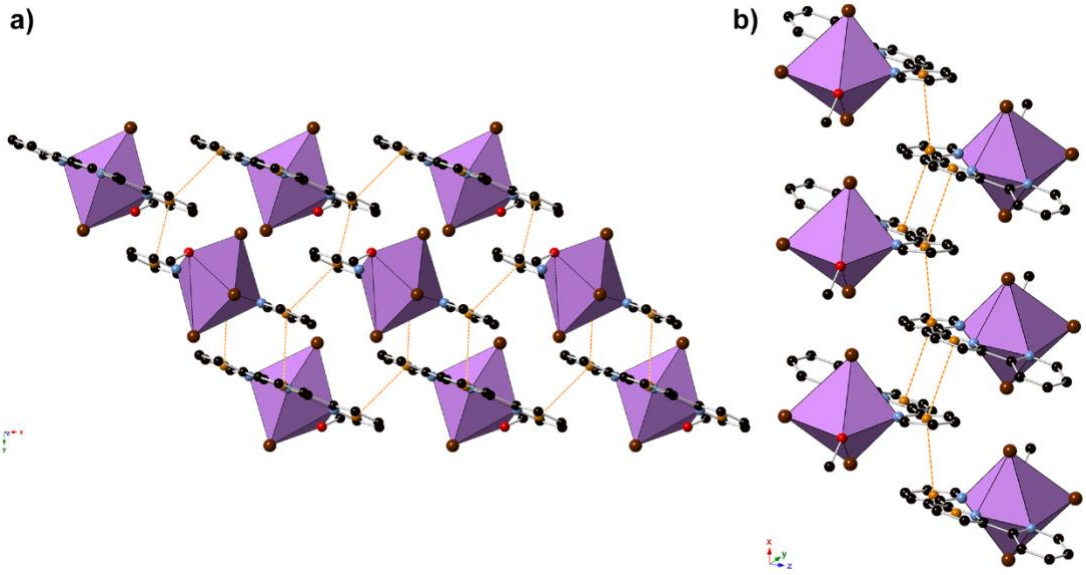

Figure S16. Packing diagrams for **5** displaying a) the 2D supramolecular sheet of Bi1 monomers and b) the 1D intermolecular chain of Bi2 monomers. Purple polyhedra represent local coordination environment of Bi metal center. Stacking interactions are rendered as orange centroid spheres and dashed lines.

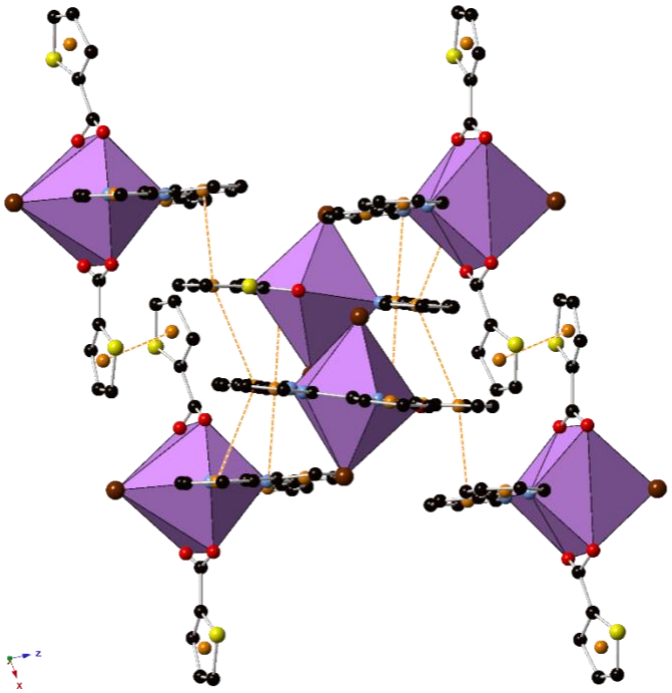

Figure S17. Packing diagram of **6** displays purple polyhedra for local coordination environment of Bi metal center. Brown, blue, black, and red spheres correspond to bromide, nitrogen, and oxygen atoms, respectively. Rendered as blue dashed lines, intermolecular Orange spheres and dashed lines are used to show centroid positions and π-π stacking interactions for specified terpy rings. Overall, these interactions construct a 3D supramolecular network.

Powder X-Ray Diffraction Patterns

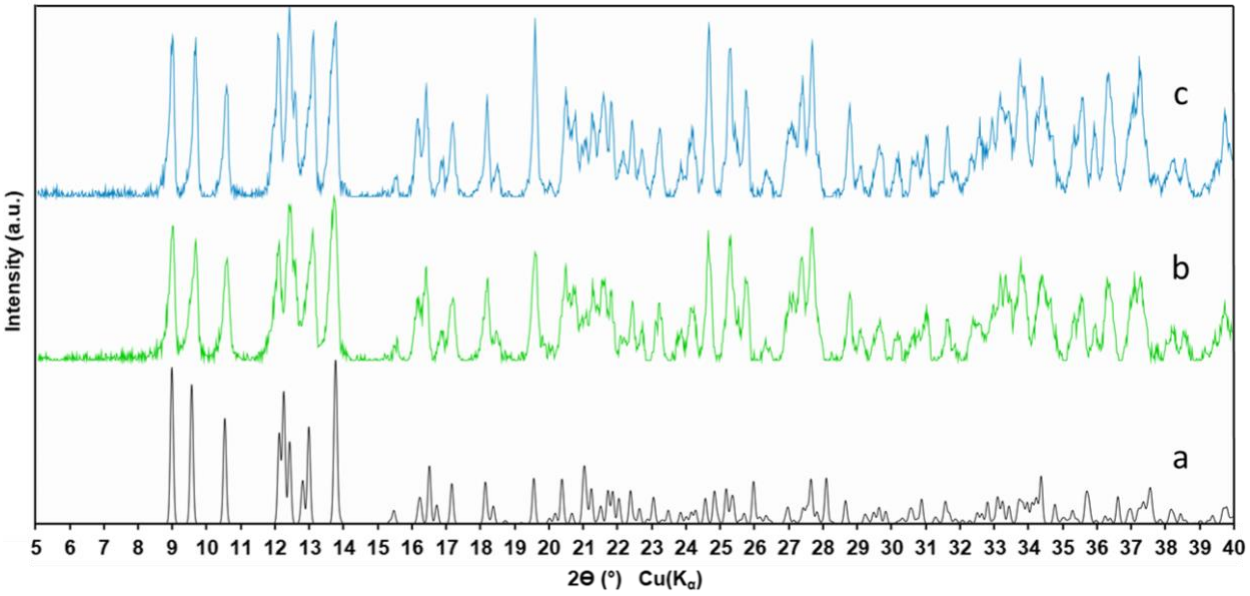

Figure S18. Calculated and experimental PXRD patterns of Compound **1**: (a) calculated pattern from SCXRD data, (b) bulk sample per reported synthesis, (c) bulk sample with TC additions without pH adjustment. Experimental diffraction patterns were acquired using Cu Kα radiation.

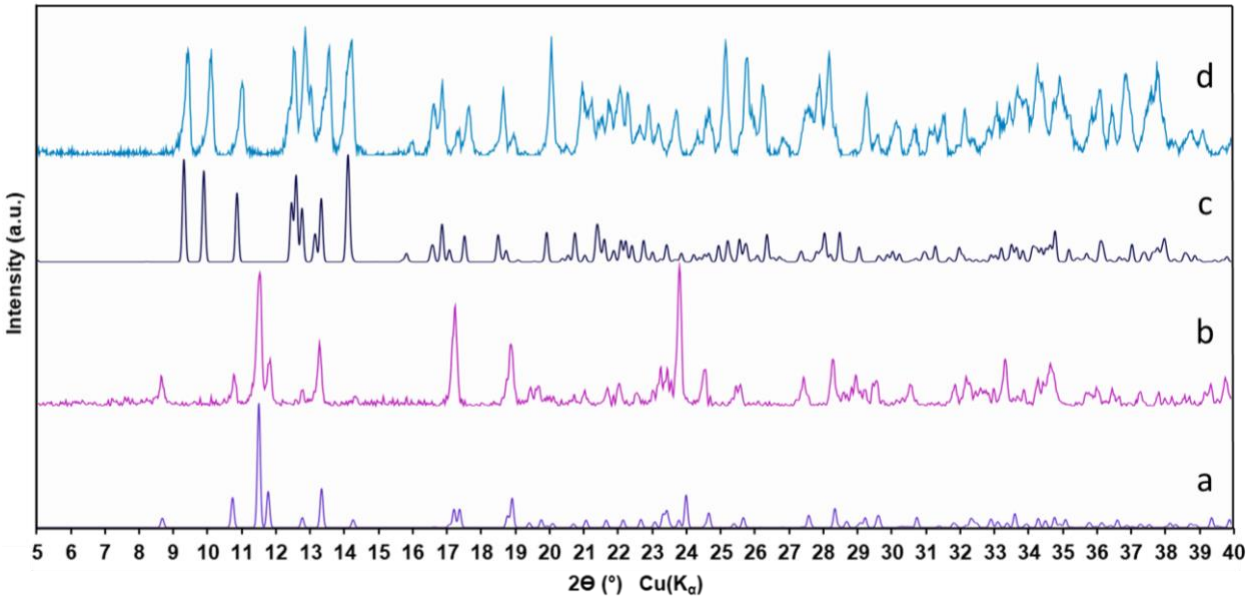

Figure S19. Calculated and experimental PXRD patterns of Compound **1** conversion to reported $[Bi_2Cl_6(terpy)_2]$ phase[1] upon acetone washing: (a) calculated pattern of $[Bi_2Cl_6(terpy)_2]$, (b) bulk sample of **1** post acetone wash, (c) calculated spectra of **1**, and (d) bulk sample of **1** pre-acetone wash. Experimental diffraction patterns were acquired using Cu Kα radiation.

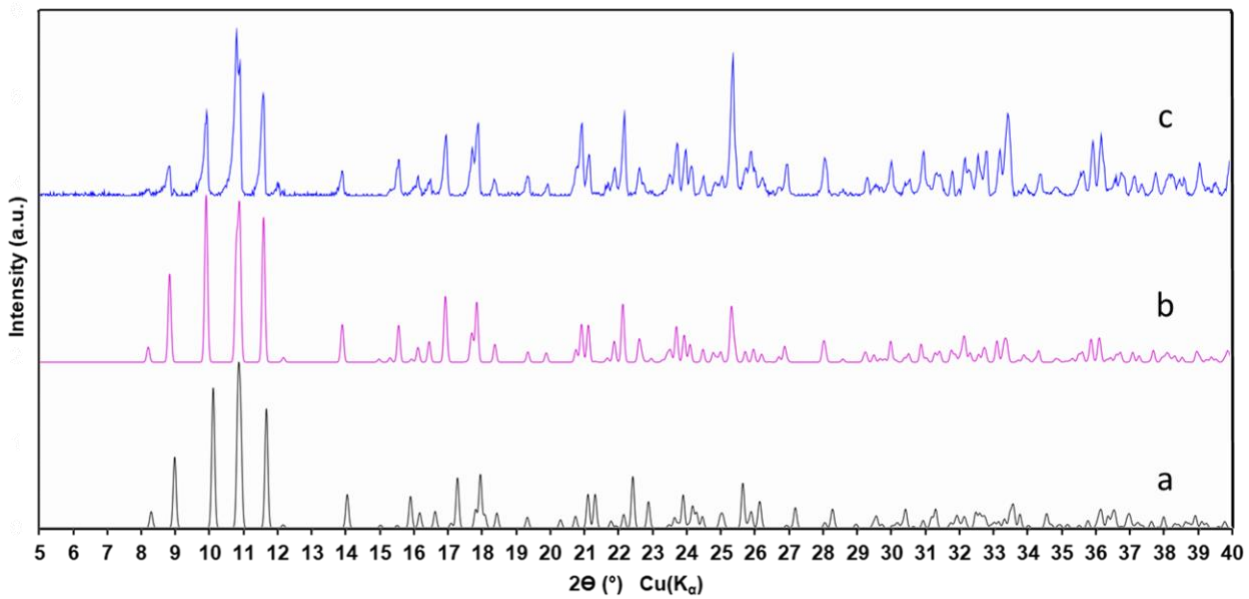

Figure S20. Calculated and experimental PXRD patterns of Compound **2**: (a) calculated pattern from SCXRD data collected at 100K, (b) Calculated pattern from SCXRD data collected at 300K, (c) bulk sample per reported synthesis. Experimental diffraction patterns were acquired using Cu Kα radiation.

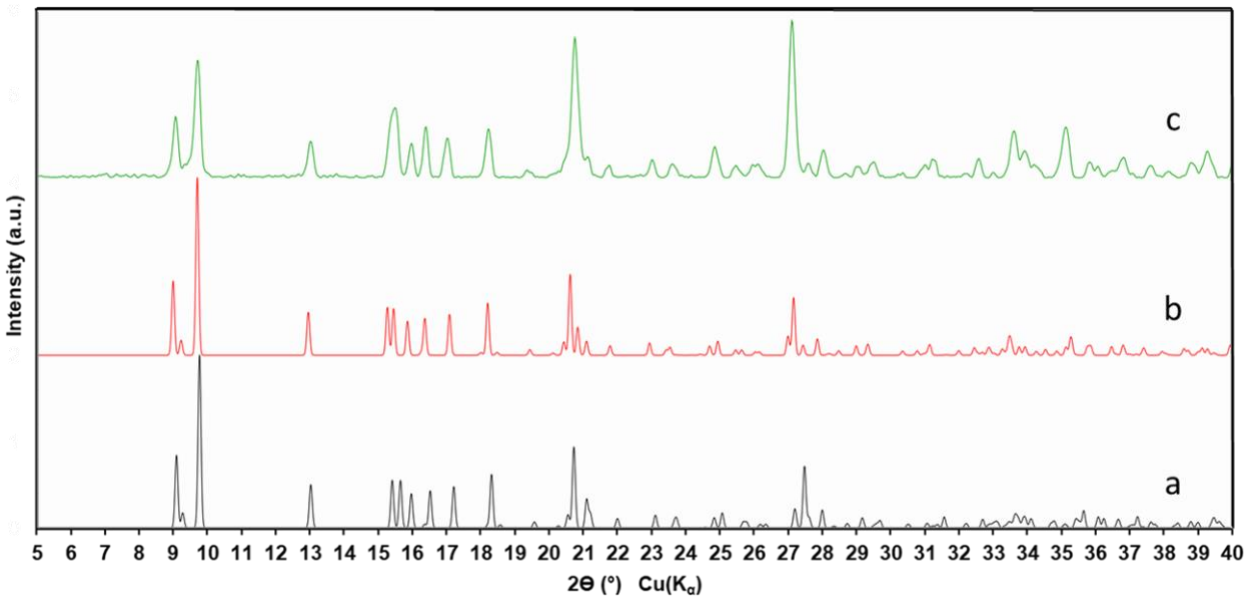

Figure S21. Calculated and experimental PXRD patterns of Compound **3A-Cl**: (a) calculated pattern from SCXRD data collected at 100K, (b) Calculated pattern from SCXRD data collected at 300K, (c) bulk sample per reported synthesis. Experimental diffraction patterns were acquired using Cu Kα radiation.

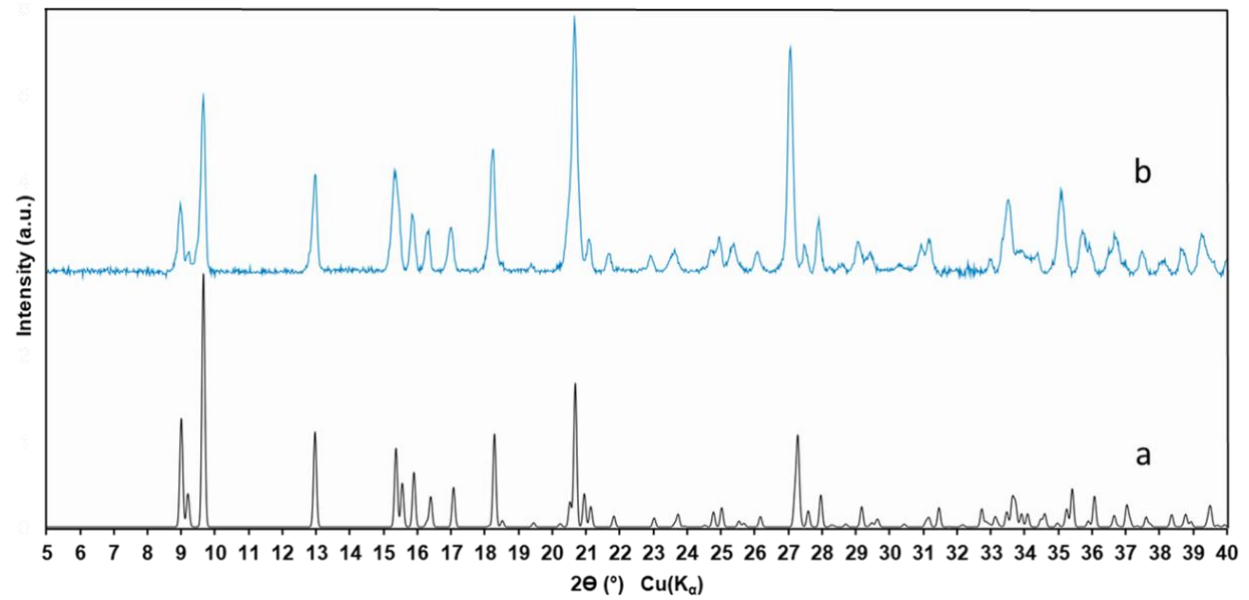

Figure S22. Calculated and experimental PXRD patterns of Compound **3A-Br**: (a) calculated pattern from SCXRD data collected at 100K, (b) bulk sample per reported synthesis. Experimental diffraction patterns were acquired using Cu Kα radiation.

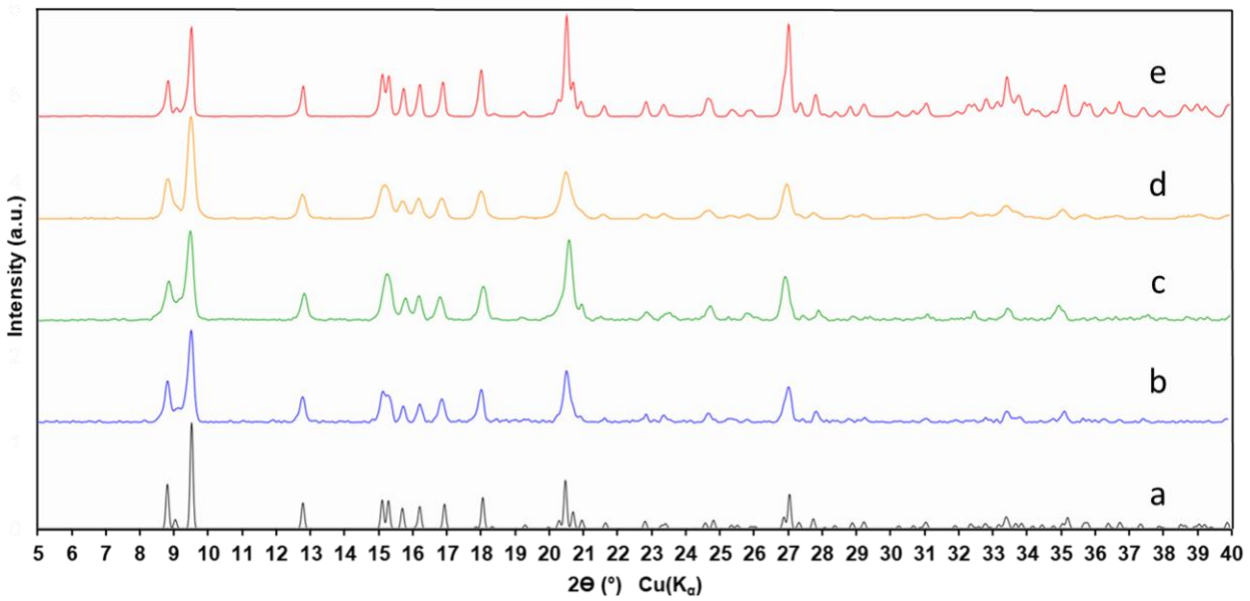

Figure S23. Calculated and experimental PXRD patterns of **3A-Bi$_{1-x}$Eu$_x$Cl** series: (a) calculated pattern for **3A-Cl** from SCXRD data collected at 300K, (b) **3A-Bi$_{0.999}$Eu$_{0.001}$Cl**, (c) **3A-Bi$_{0.995}$Eu$_{0.005}$Cl**, (d) **3A-Bi$_{0.99}$Eu$_{0.01}$Cl**, (e) **3A-Bi$_{0.95}$Eu$_{0.05}$Cl** acquired using Cu Kα radiation.

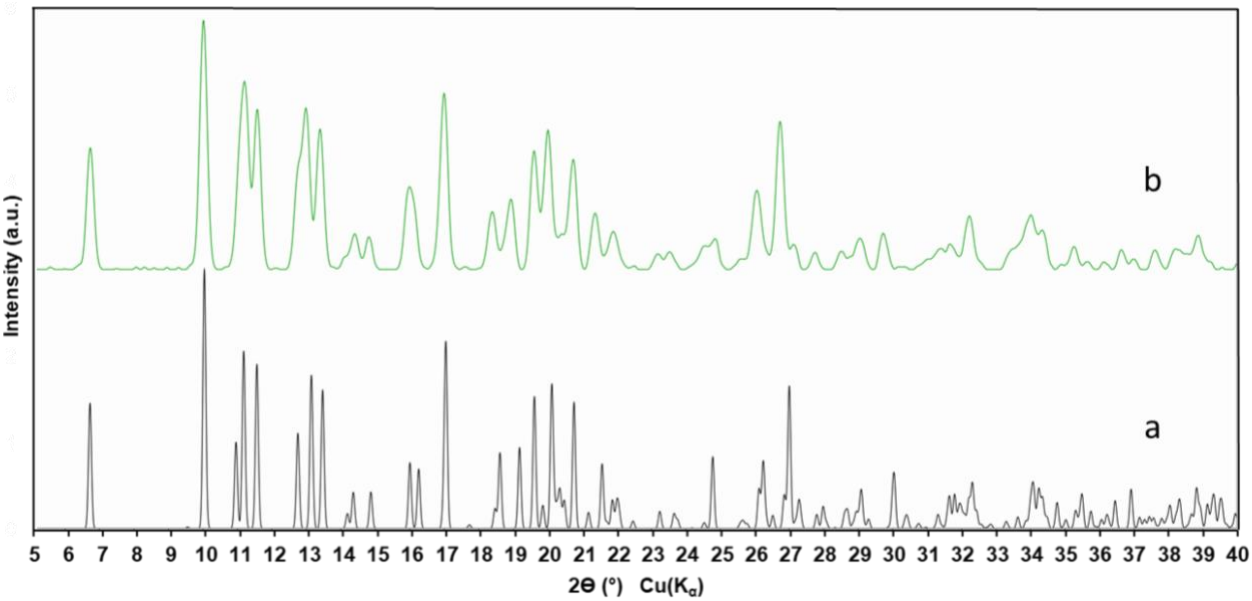

Figure S24. Calculated and experimental PXRD patterns of Compound **3B-Cl**: (a) calculated pattern from SCXRD data collected at 100K, (b) bulk sample of **3B-Cl** per reported synthesis. Experimental diffraction patterns were acquired using Cu Kα radiation.

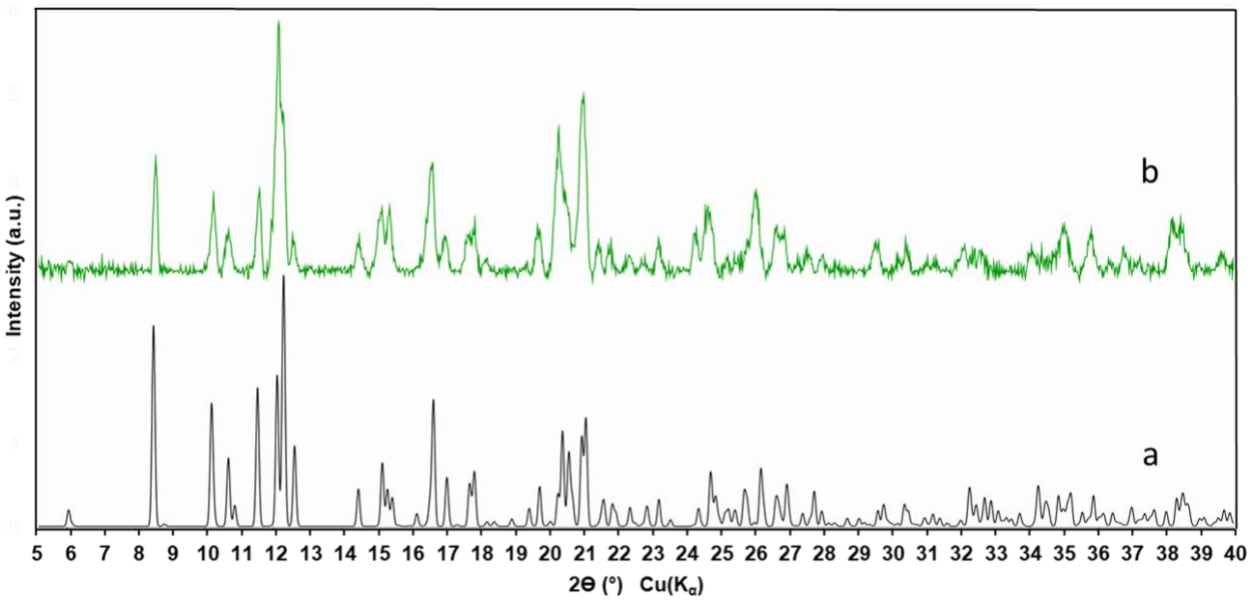

Figure S25. (a) Calculated and (b) experimental PXRD pattern of **4** bulk sample. Experimental diffraction patterns were acquired using Cu Kα radiation.

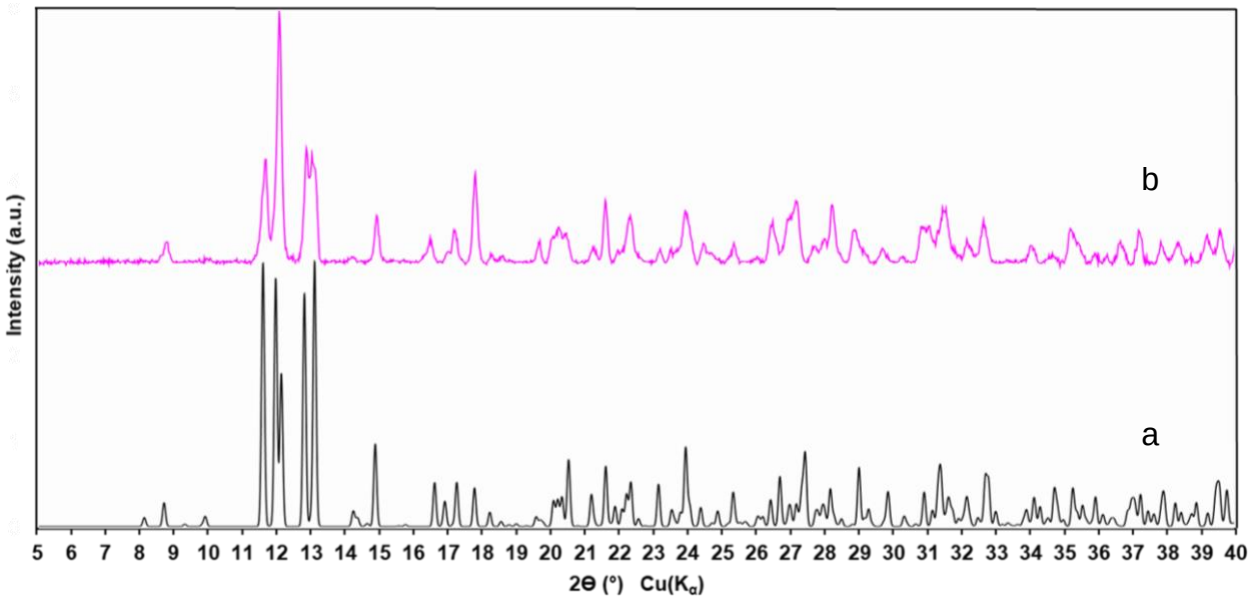

Figure S26. (a) Calculated and (b) experimental PXRD pattern of **5** bulk sample. Experimental diffraction patterns were acquired using Cu Kα radiation.

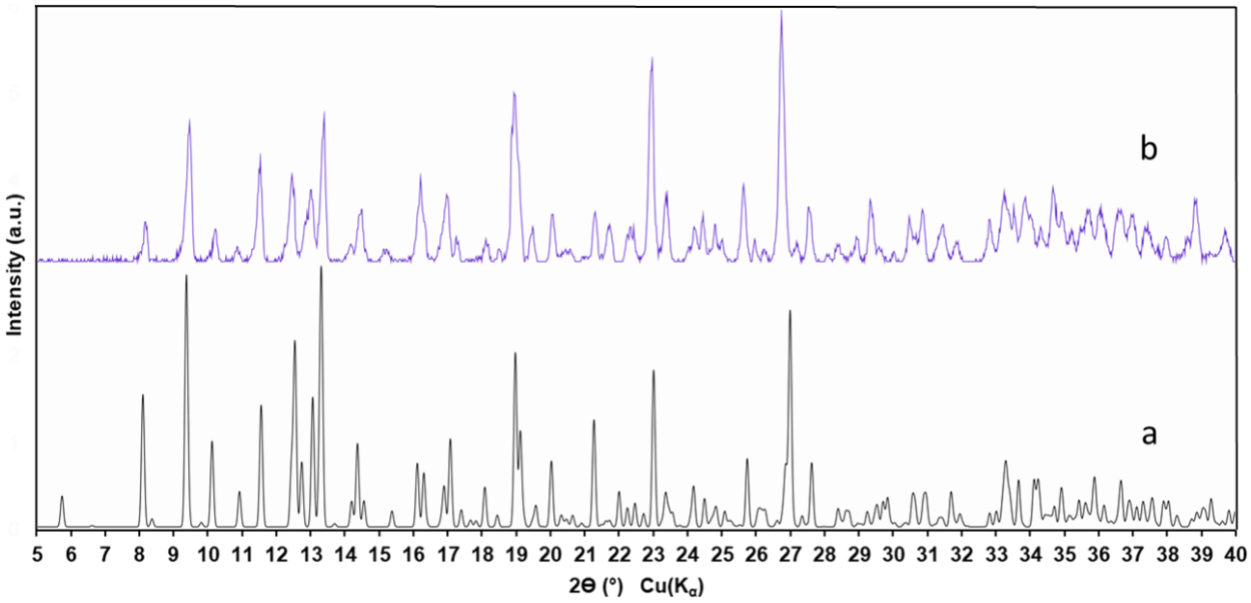

Figure S27. (a) Calculated and (b) experimental PXRD pattern of **6** bulk sample. Experimental diffraction patterns were acquired using Cu Kα radiation.

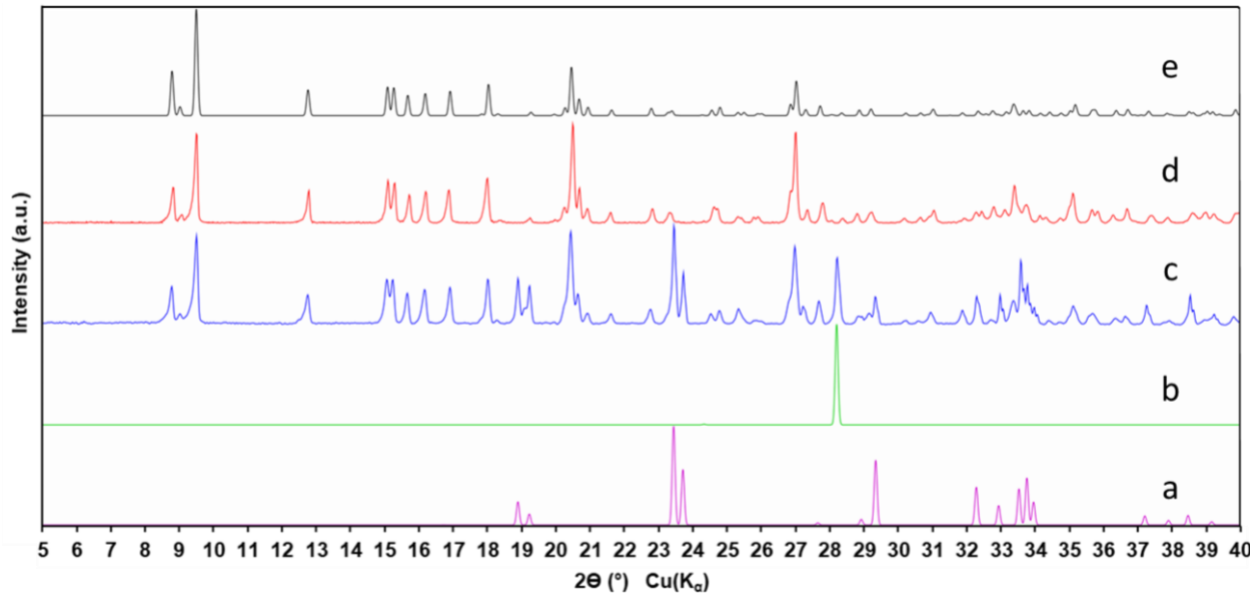

Figure S28. Diffraction spectra comparison of **3A-$Bi_{0.95}Eu_{0.05}Cl$** pre- and post-washings in attempts to remove acknowledged impurities. Spectra are as followed: (a) KNO_3 ICSD-28077, (b) KCl ICSD-28938, (c) pre-washed **3A-$Bi_{0.95}Eu_{0.5}Cl$**, (d) post-washed **3A-$Bi_{0.95}Eu_{0.5}Cl$**, (e) calculated pattern of **3A-Cl** collected at 300K.

Phase Purity Issue

For phases exhibiting aforementioned impurities (**3A-Cl**, **3A-Bi$_{0.999}$Eu$_{0.001}$Cl**, **3A-Bi$_{0.995}$Eu$_{0.005}$Cl**, **3A-Bi$_{0.99}$Eu$_{0.01}$Cl**, **3A-Bi$_{0.95}$Eu$_{0.05}$Cl**, and **3B-Cl**) the following efforts were made to ensure bulk luminescent behavior could be confidently attributed to targeted phases with no influence of impurities. Displayed in Figure S36, comparison of relative emission intensity reveals no appreciable emission was observed for KNO_3 and KCl mixture at an excitation wavelength of 420 nm as compared to bulk **3A-Cl**, **3A-Bi$_{0.999}$Eu$_{0.001}$Cl**, and **3B-Cl** samples. Identical instrumental settings (2 nm slit widths) and slide preparations were employed for these emission collections. Additionally, single crystals for **3A-Cl**, **3A-Bi$_{0.999}$Eu$_{0.001}$Cl**, **3A-Bi$_{0.995}$Eu$_{0.005}$Cl**, **3A-Bi$_{0.99}$Eu$_{0.01}$Cl**, **3A-Bi$_{0.95}$Eu$_{0.05}$Cl**, and **3B-Cl** were manually separated from bulk product and diluted into a PMMA matrix at a weight ratio of 1:50. These diluted samples were analyzed under the same instrument settings as the bulk studies to further rule out any potential influences on luminescent behavior by trace impurities. No appreciable differences in excitation or emission profile was observed for bulk product verses single crystal PMMA samples. Emission CIE coordinates were also determined for the PMMA diluted single crystal mixtures. These coordinates were found to be identical within certainty to those of bulk product, further assuring observed luminescent behavior originates from targeted phases with no measurable influence of any trace impurities. To further confirm observed emissive behavior originated from targeted phases, emission spectra for individual singles for compounds **3A-Cl**, **3A-Bi$_{0.999}$Eu$_{0.001}$Cl**, **3A-Bi$_{0.995}$Eu$_{0.005}$Cl**, and **3A-Bi$_{0.99}$Eu$_{0.01}$Cl** were acquired via laser spectroscopy by utilizing the aforementioned Horiba LabRAM microscope, its spectroscopic capabilities, and available 405 nm laser light source. Falling within the window of observe sample excitation, the 405 nm laser enable the collection of single crystal emission spectra which are shown in Figure S35. Acquisition settings for these collections were as followed: 20 acquisitions, 1 second incident light exposure, spectral window of 425-800 nm and a laser power of 0.1-1%. Observed emissive profiles of crystals exhibited contributions of both ligand/BiX and Eu emission, as seen in bulk sample. Moreover, Eu emission intensity was observed to became more dominant with increasing Eu doping, trending with bulk preparations. Unfortunately, single crystal emission spectra useful for comparison could not be reliably collected for **3A-Bi$_{0.95}$Eu$_{0.05}$Cl** due to oversaturation of the detector even when employing lowest laser power settings. Nevertheless, such reflections of emissive features and trends within bulk product, manually separated crystalline PMMA dilutions, and individual single crystals of targeted phases ensures that they are responsible for observed luminescence with negligible or no influence from any trace impurities.

Raman spectroscopic studies of individual crystals for **3A-Cl**, **3A-Bi$_{0.999}$Eu$_{0.001}$Cl**, and **3A-Bi$_{0.995}$Eu$_{0.005}$Cl** reveal identical vibration transition in the range of 200-1700 cm^{-1}; however, intense harmonic $^5D_0 \rightarrow {}^7F_j$ Eu emissions were observed in doped phases, Figure S48-S49. These harmonic emissions overwhelmed vibrational spectra; however, provide interesting insight into Eu composition within these doped single crystals. While the presence of these transitions affirm Eu is present within this single phase, identical peak positions and splitting for these transitions suggest common Eu coordination environment between these samples, as expected for Bi site substitution.

Additional Luminescence and Optical Data

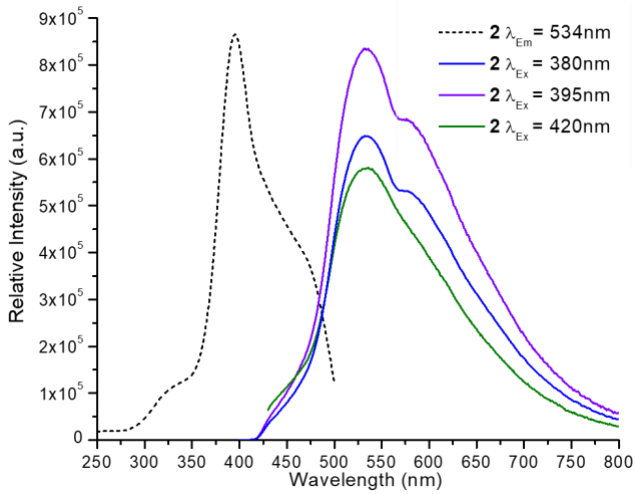

Figure S29. Excitation (λ_{Em} = 533 nm) and emission (λ_{Ex} = 380, 395, and 420 nm) spectra for **2**.

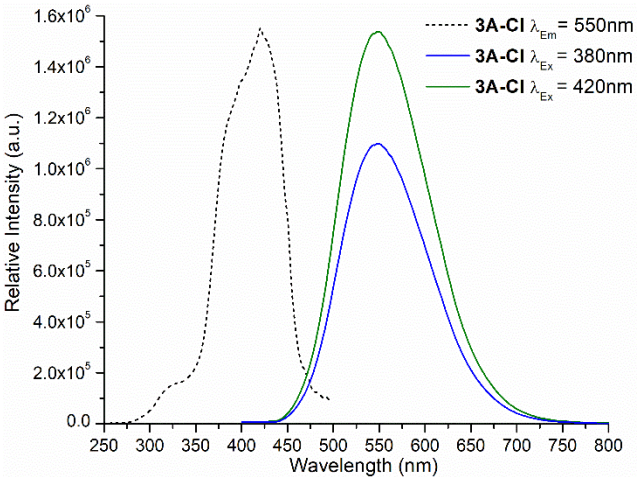

Figure S30. Excitation (λ_{Em} = 533 nm) and emission (λ_{Ex} = 380 and 420 nm) spectra for **3A-Cl**.

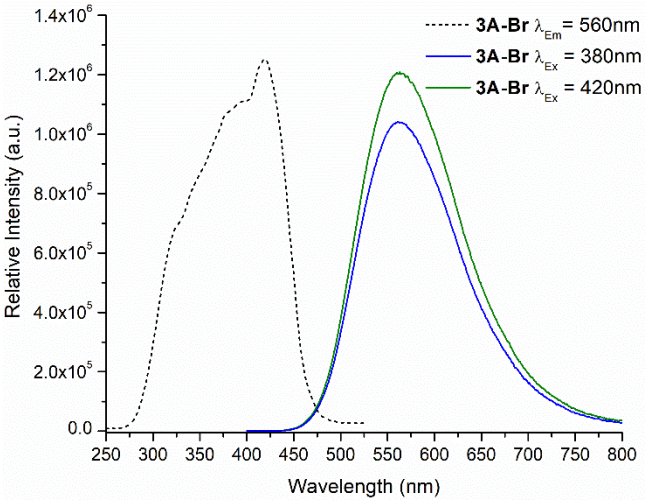

Figure S31. Excitation (λ_{Em} = 533 nm) and emission (λ_{Ex} = 380 and 420 nm) spectra for **3A-Br**.

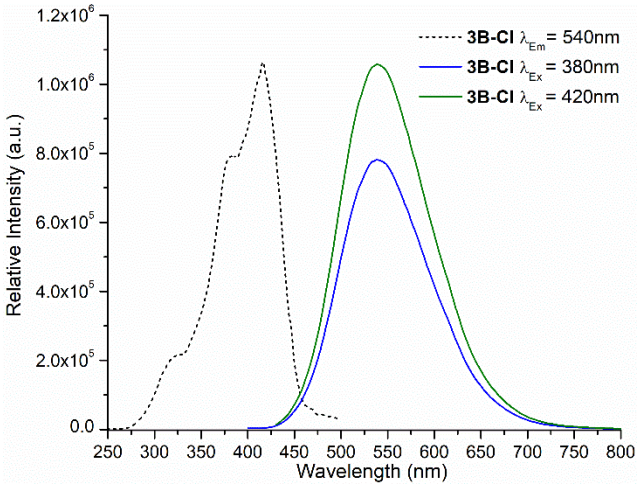

Figure S32. Excitation (λ_{Em} = 533 nm) and emission (λ_{Ex} = 380 and 420 nm) spectra for **3B-Cl**.

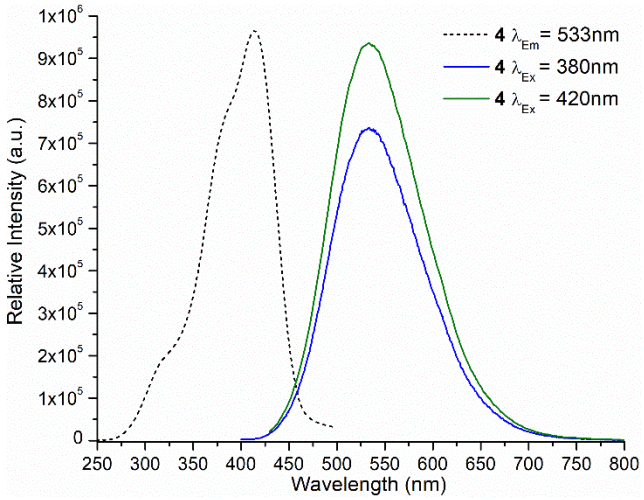

Figure S33. Excitation (λ_{Em} = 533 nm) and emission (λ_{Ex} = 380 and 420 nm) spectra for **4**.

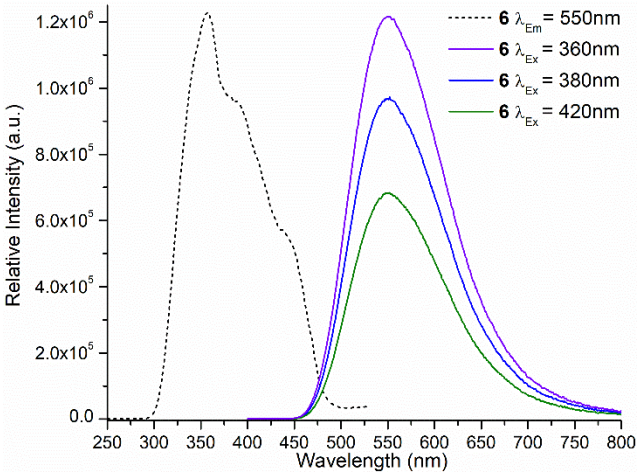

Figure S34. Excitation (λ_{Em} = 550 nm) and emission (λ_{Ex} = 360, 380, and 420 nm) spectra for **6**.

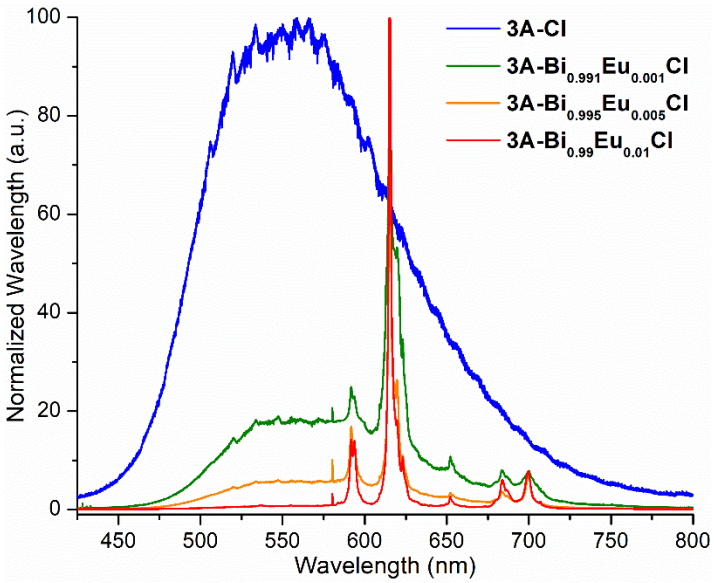

Figure S35. Normalized single crystal emission spectra (λ_{Ex} = 405 nm) for **3A-Cl**, **3A-Bi$_{0.999}$Eu$_{0.001}$Cl**, **3A-Bi$_{0.995}$Eu$_{0.005}$Cl**, and **3A-Bi$_{0.99}$Eu$_{0.01}$Cl** via laser spectroscopy.

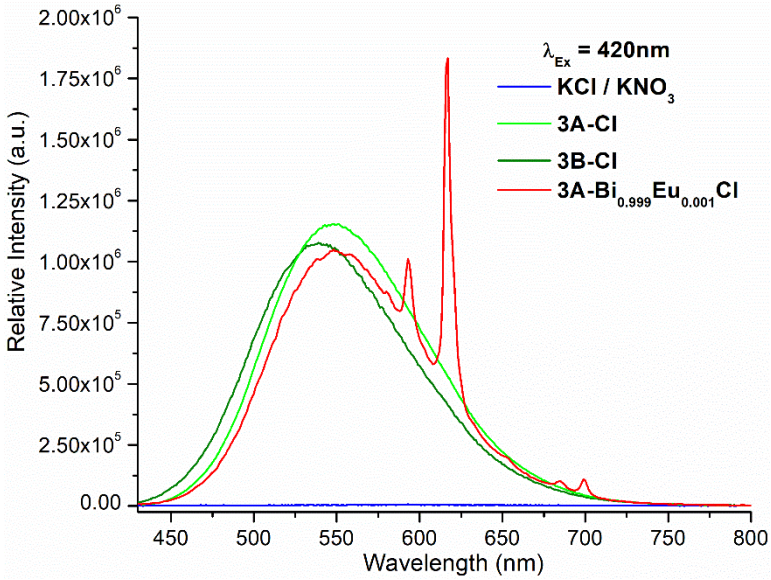

Figure S36. Comparison of relative emission for **3A-Cl**, **3A-Bi$_{0.999}$Eu$_{0.001}$Cl**, **3B-Cl**, and a 50:50 mixture of KCl and KNO_3 under identical sample quantities (5mg), instrument settings (2 nm slit widths), and excitation wavelengths (λ_{Ex} = 420 nm).

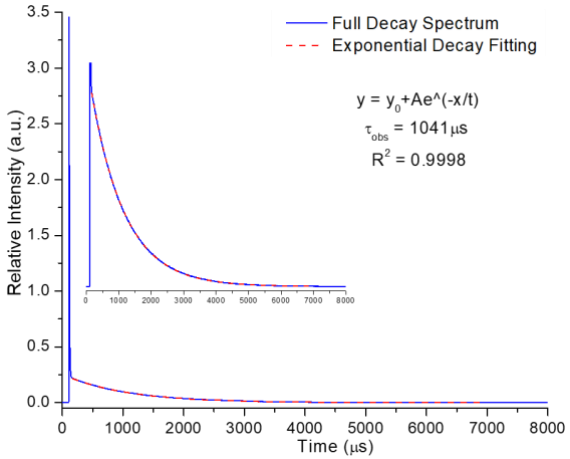

Figure S37. Lifetime decay curve of **3A-$Bi_{0.995}Eu_{0.005}Cl$** emission at 616 nm upon irradiation at λ_{Ex} = 420 nm. Initial fast decay at 110-150μs corresponds to LXMCT/ligand decay (<10μs). Inset provided for clarity of long decay.

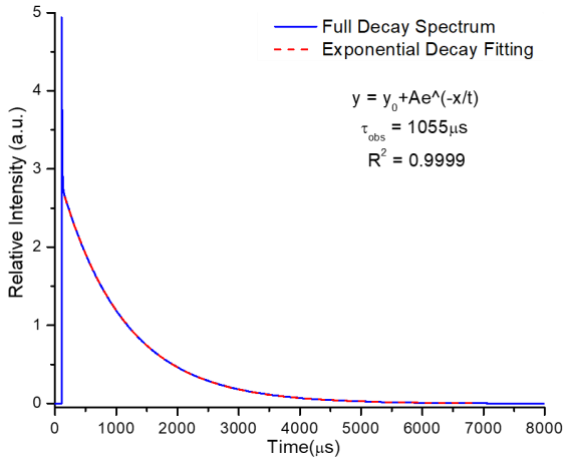

Figure S38. Lifetime decay curve of **3A-$Bi_{0.99}Eu_{0.01}Cl$** emission at 616 nm upon irradiation at λ_{Ex} = 420 nm. Initial fast decay at 110-150μs corresponds to LXMCT/ligand decay (<10μs).

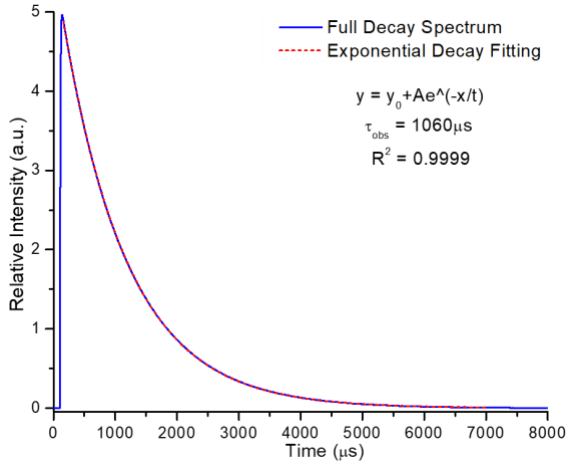

Figure S39. Lifetime decay curve of **3A-$Bi_{0.95}Eu_{0.05}Cl$** emission at 616 nm upon irradiation at λ_{Ex} = 420 nm. Lack of initial decay at 110-150 demonstrates dominance of Eu emission.

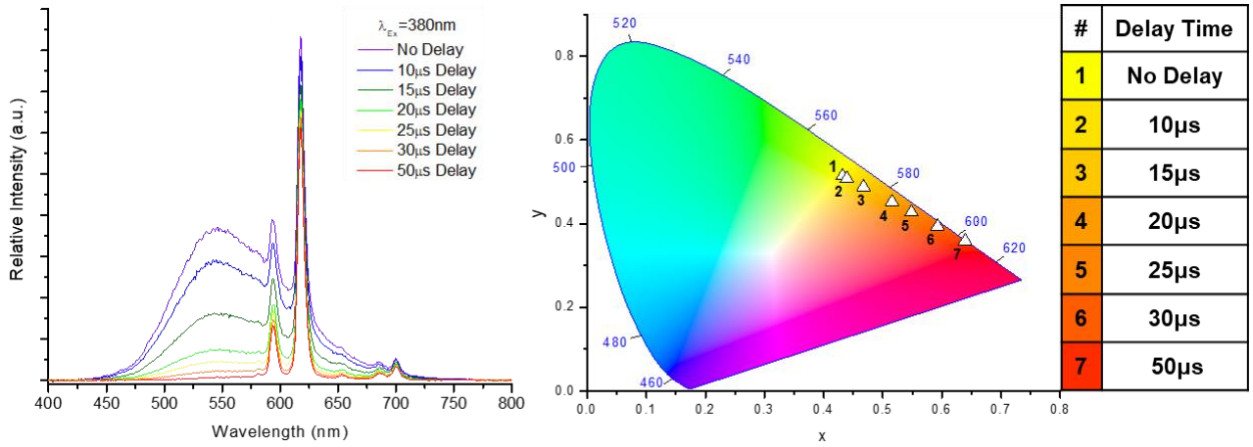

Figure S40. Room Temperature Time-Resolved Spectra for **3A-Bi$_{0.999}$Eu$_{0.001}$Cl** with varied time delay. Ligand based emission (~550 nm) is extinct after 50μs, while Eu emissions (λ_{max}= 616 nm) retained. Resultant changes in chromaticity are shown in 1931 CIE plot with corresponding legend. CIE positions are symbolized by numbered white triangles.

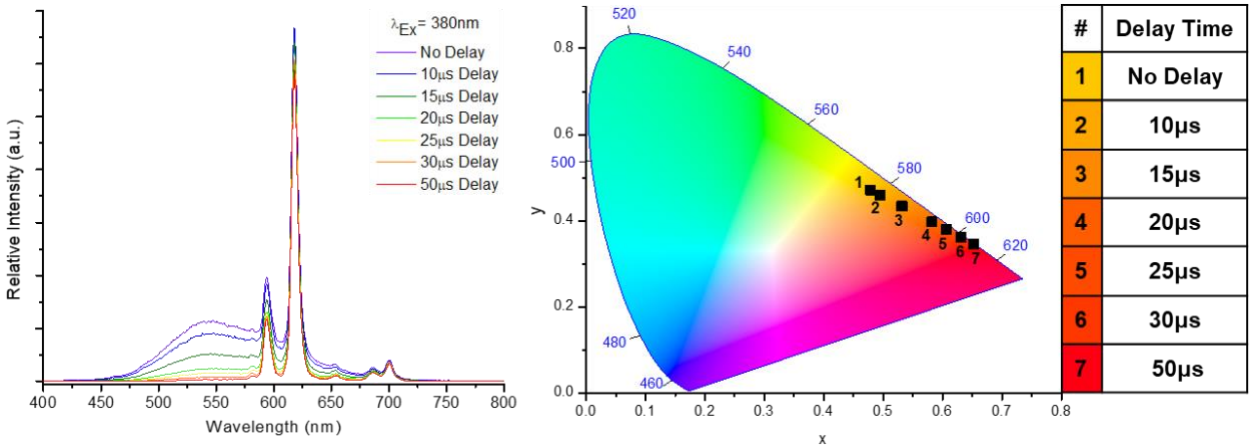

Figure S41. Room Temperature Time-Resolved Spectra for **3A-Bi$_{0.995}$Eu$_{0.005}$Cl** with varied time delay. Ligand based emission (~550 nm) is extinct after 50μs, while Eu emissions (λ_{max}= 616 nm) retained. Resultant changes in chromaticity are shown in 1931 CIE plot with corresponding legend. CIE positions are symbolized by numbered black squares.

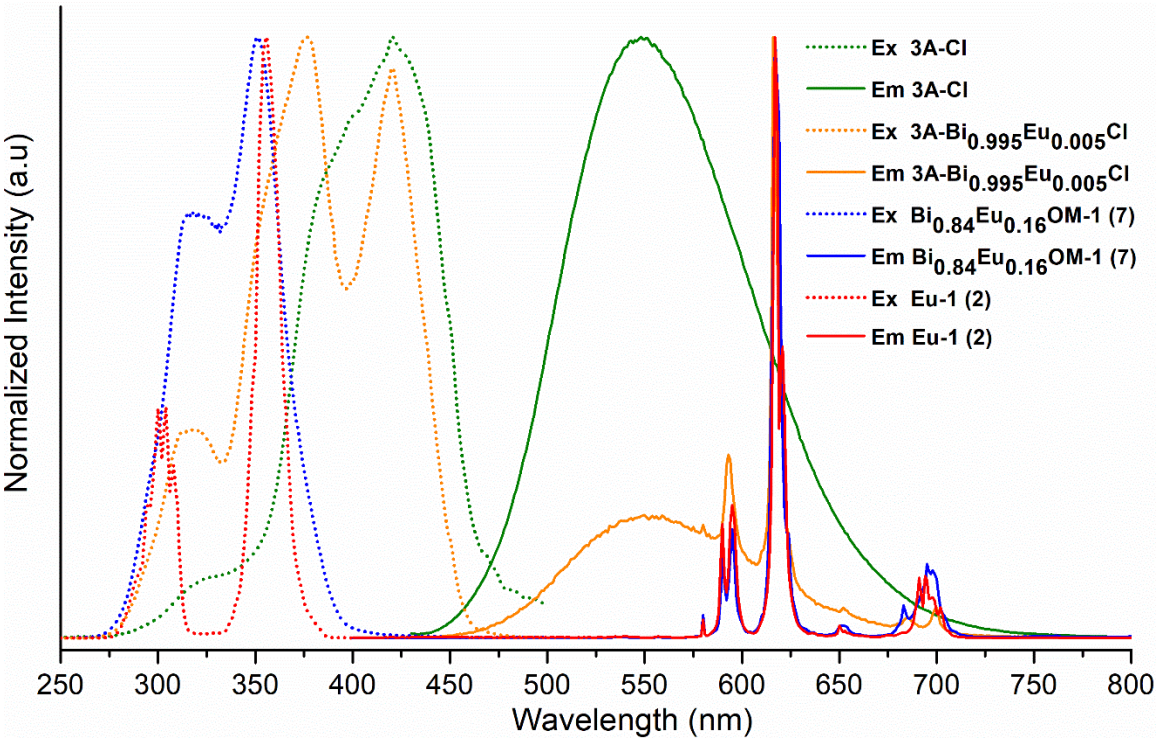

Figure S42. Excitation and emission spectra comparison of **3A-Cl** and **3A-Bi$_{0.995}$Eu$_{0.005}$Cl** (from this work) to **Bi$_{0.84}$Eu$_{0.16}$OM-1** (from Batrice et al.[7]) and **Eu-1** (from Knope et al.[2]). Notably, visible excitation is present in **3A-Cl** and **3A-Bi$_{0.995}$Eu$_{0.005}$Cl**; while near analogous compounds, with no halides, **Bi$_{0.84}$Eu$_{0.16}$OM-1** and **Eu-1** do not possess this luminescent behavior.

Figure S43. Images of bulk sample luminescence under a UV handlamp for **3A-Cl**, **3A-Bi$_{0.999}$Eu$_{0.001}$Cl**, **3A-Bi$_{0.995}$Eu$_{0.005}$Cl**, **3A-Bi$_{0.9}$Eu$_{0.01}$Cl**, and **3A-Bi$_{0.95}$Eu$_{0.05}$Cl** (displayed from left to right, respectively).

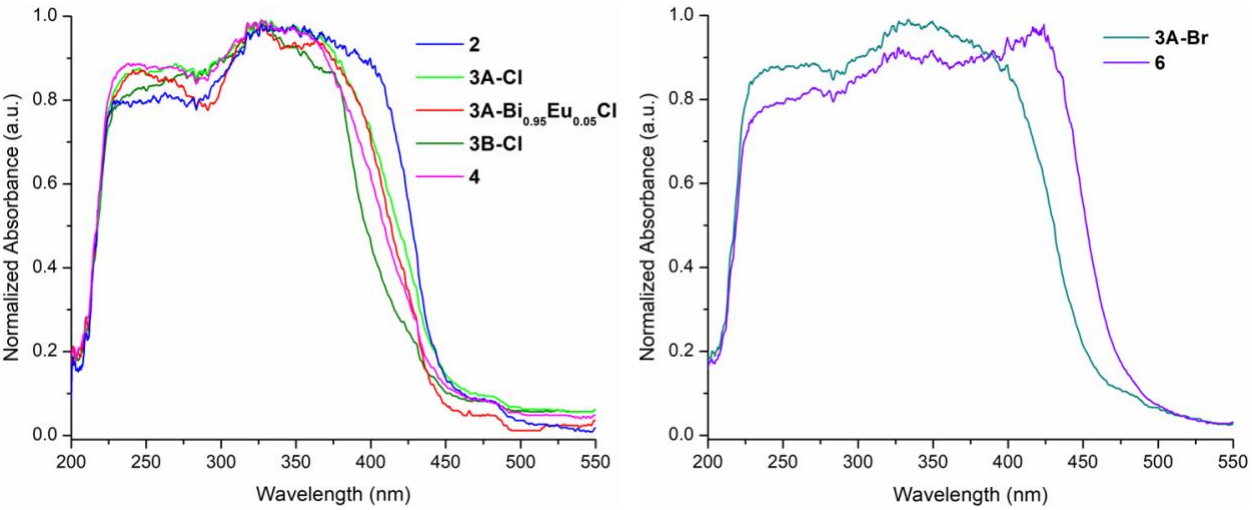

Figure S44. UV Absorbance data for luminescent BiCl phases (left) and BiBr phases (right) which demonstrate similar shape and extension of absorbance into the visible range (>400 nm). Spectra were displayed from 200-550 nm for clarity.

Raman Spectra

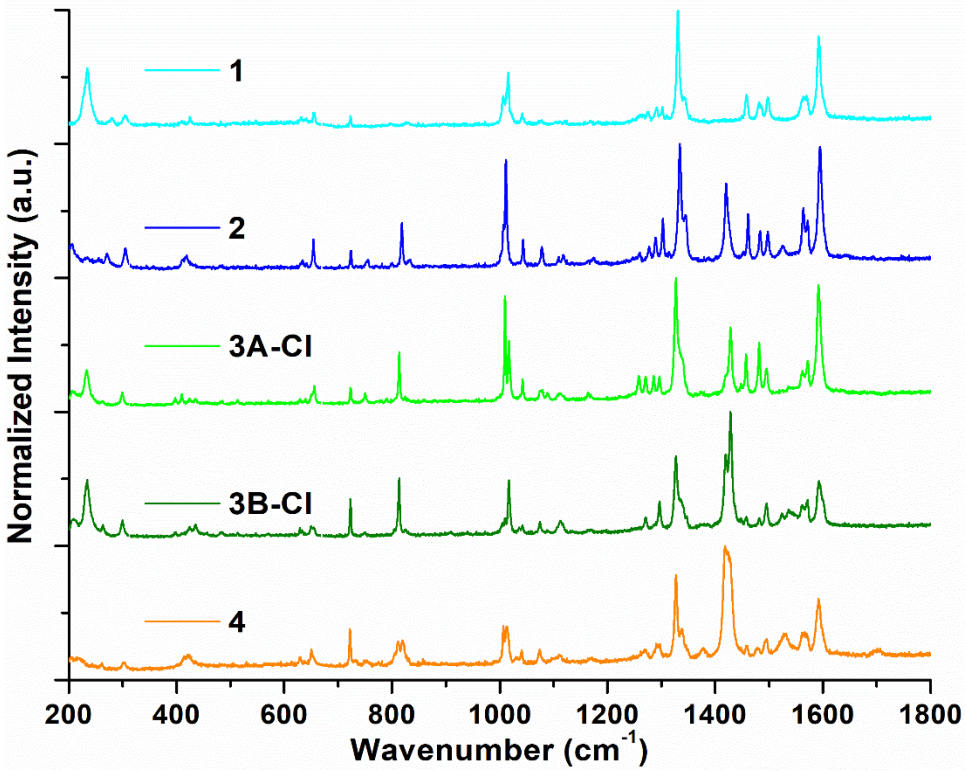

Figure S45. Compiled Raman spectra for compounds **1**, **2**, **3A-Cl**, **3B-Cl**, and **4**. Spectra are limited from 200-1800 cm^{-1} for clarity of principal transitions.

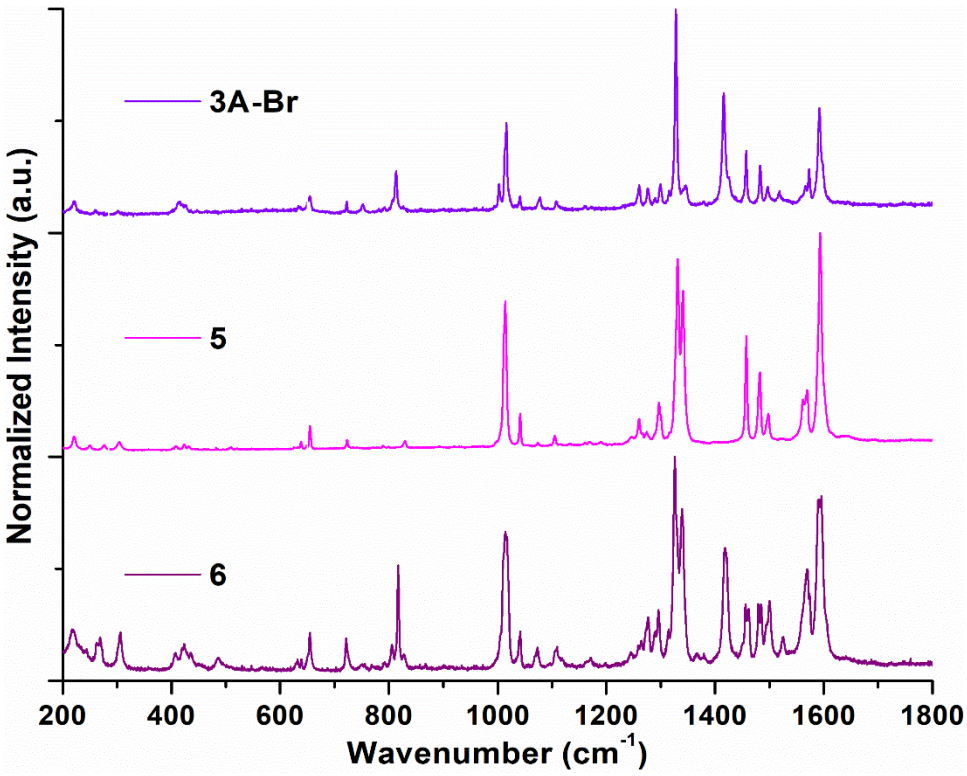

Figure S46. Compiled Raman spectra for compounds **3A-Br**, **5**, and **6**. Spectra are limited from 200-1800 cm^{-1} for clarity of principal transitions.

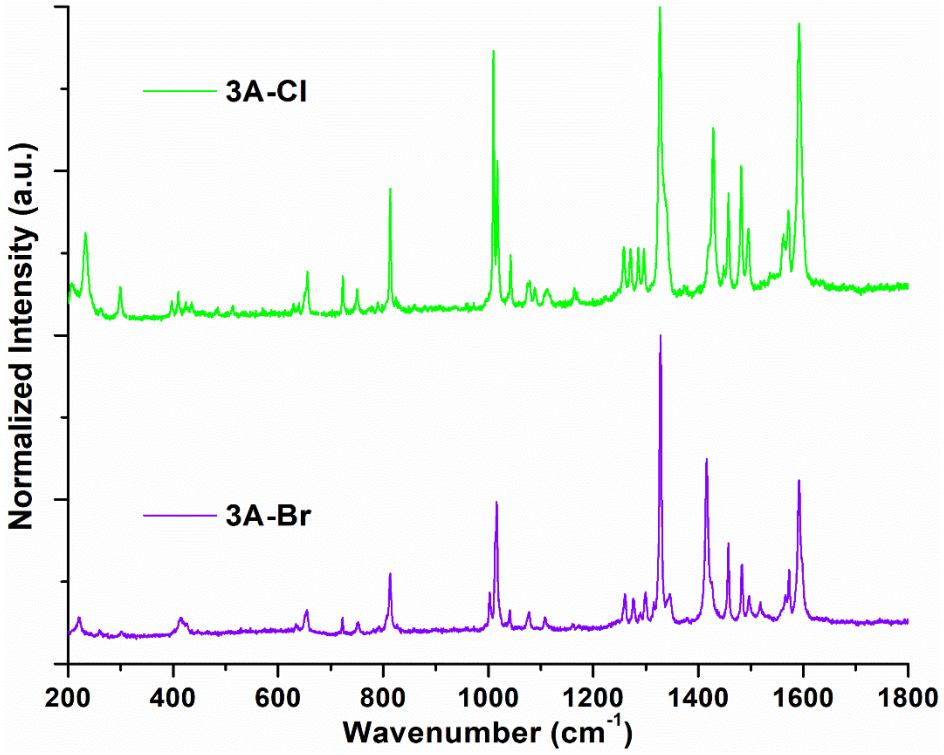

Figure S47. Comparison of Raman spectra for **3A-Cl** and **3A-Br**.

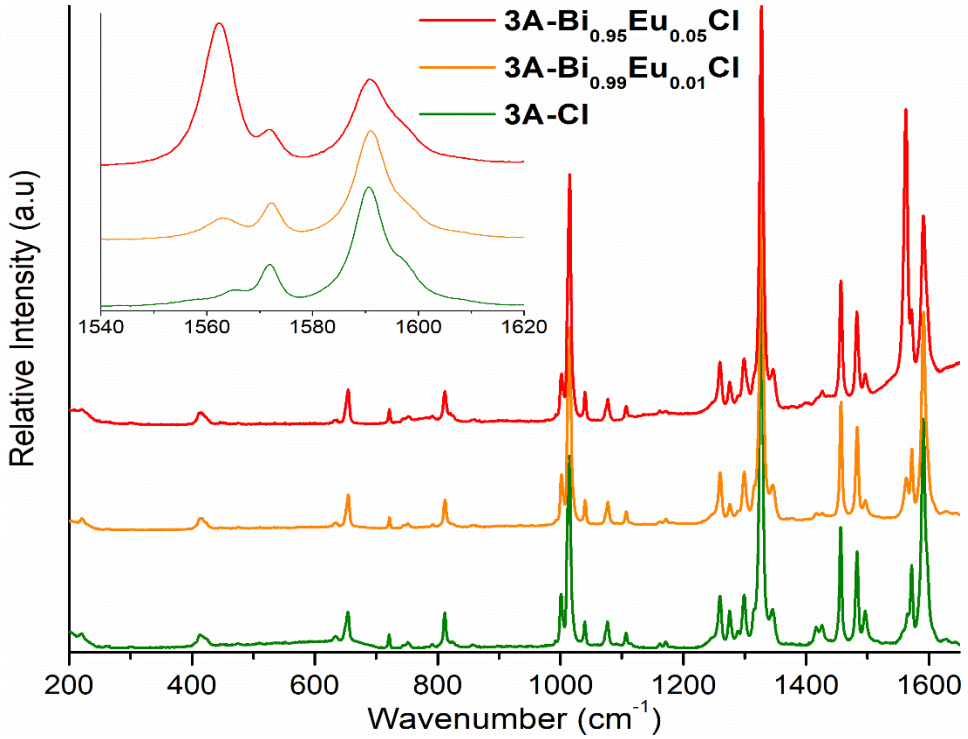

Figure S48. Stacked Raman spectra of **3A-Cl**, **3A-Bi$_{0.99}$Eu$_{0.01}$Cl**, and **3A-Bi$_{0.95}$Eu$_{0.05}$Cl**. Inset spectra highlights the 11th harmonic of the $^5D_0 \rightarrow {}^7F_0$ emissive transition (582 nm = 17,182 cm^{-1}) centered at 1562 cm^{-1}. Notably, intensity of this transition grows with increasing Eu doping percentage. Spectra are limited from 200-1620 cm^{-1} for clarity of principal transitions.

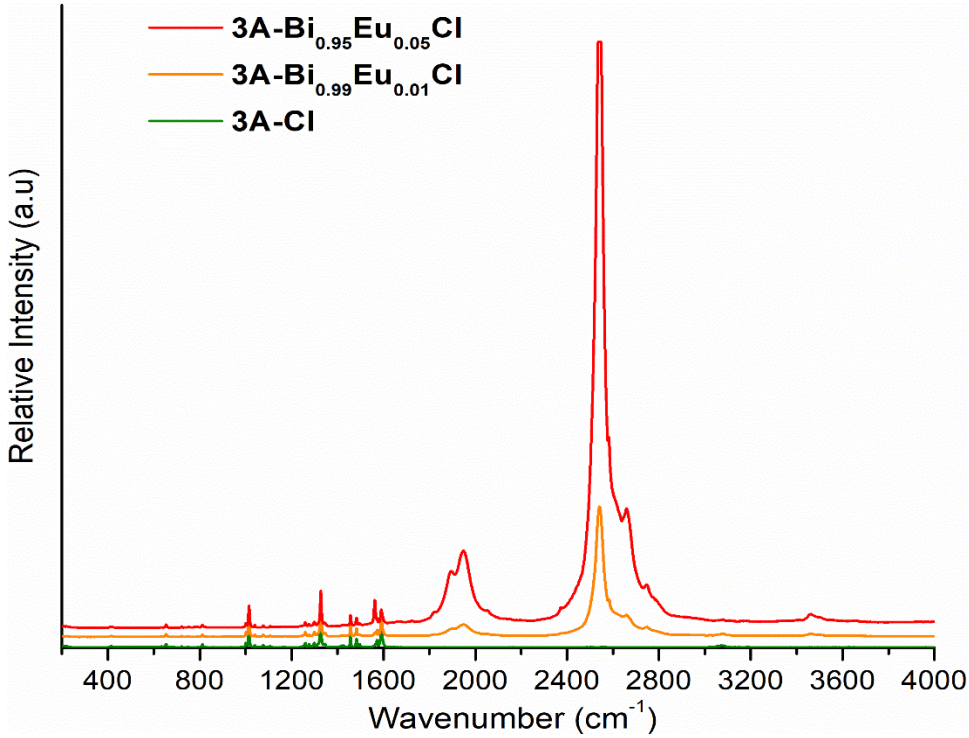

Figure S49. Extended Raman spectra of those shown in Figure S48 further displaying influence of $^5D_0 \rightarrow {}^7F_j$ harmonic transitions. 532 nm laser used for incident beam.

Additional Computational Data

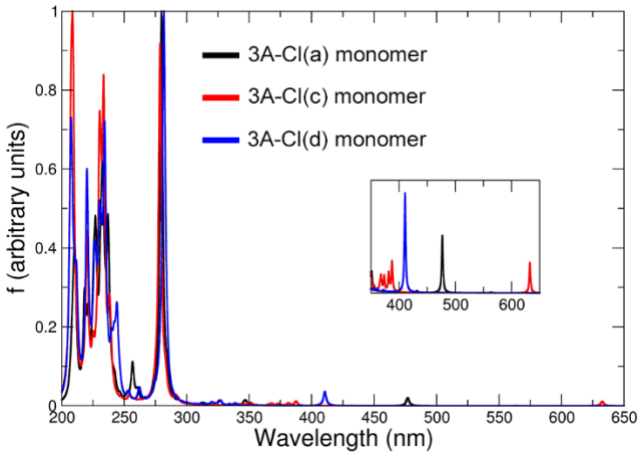

Figure S50. Calculated Absorbance Spectra for **3A-Cl(a)**, **3A-Cl(c)**, and **3A-Cl(d)** derivatives that possess general formulas $BiCl(terpy)(TC)_2$, $BiCl_2(terpy)(TC)$, and $Bi(terpy)(TC)_3$, respectively.

Table S5. Absorption energies of frontier orbital transitions for **3A-Cl(a)**, **3A-Cl(c)**, and **3A-Cl(d)**. Corresponding to Figures S51-53, orbital model (OM) numbers for each structural derivative are denoted for occupied (Occ.) and virtual (V.) orbital contributions.

State	3A-Cl(a) Energy		Figure S51 OM		3A-Cl(c) Energy		Figure S52 OM		3A-Cl(d) Energy		Figure S53 OM	
	(eV)	(nm)	Occ.	V.	(eV)	(nm)	Occ.	V.	(eV)	(nm)	Occ.	V.
1	2.60	477	9	1	1.96	633	6	1	3.03	410	10 8, 9	1
2	2.87	432	9	2	2.20	564	6	2	3.33	373	10 8, 9	2
3	3.27	379	6 5, 8	1	3.20	387	4	1	3.45	359	6, 3 8	1
4	3.53	351	1 5, 6	1	3.25	381	3	1	3.53	351	2, 4 7	1
5	3.57	348	3 4, 6	1	3.31	374	2	1	3.66	339	1 6, 9	1
6	3.58	346	6 1, 3	2 1	3.36	368	6	3	-	-	-	-
7	3.63	341	2 1, 8	1	3.38	366	1	1	-	-	-	-
8	3.71	334	8 6, 7	1	3.48	355	4	2	-	-	-	-
9	-	-	-	-	3.52	352	6	4	-	-	-	-
10	-	-	-	-	3.55	349	3	2	-	-	-	-
11	-	-	-	-	3.60	344	2	2	-	-	-	-
12	-	-	-	-	3.66	338	1	2	-	-	-	-
13	-	-	-	-	3.85	322	5	1				

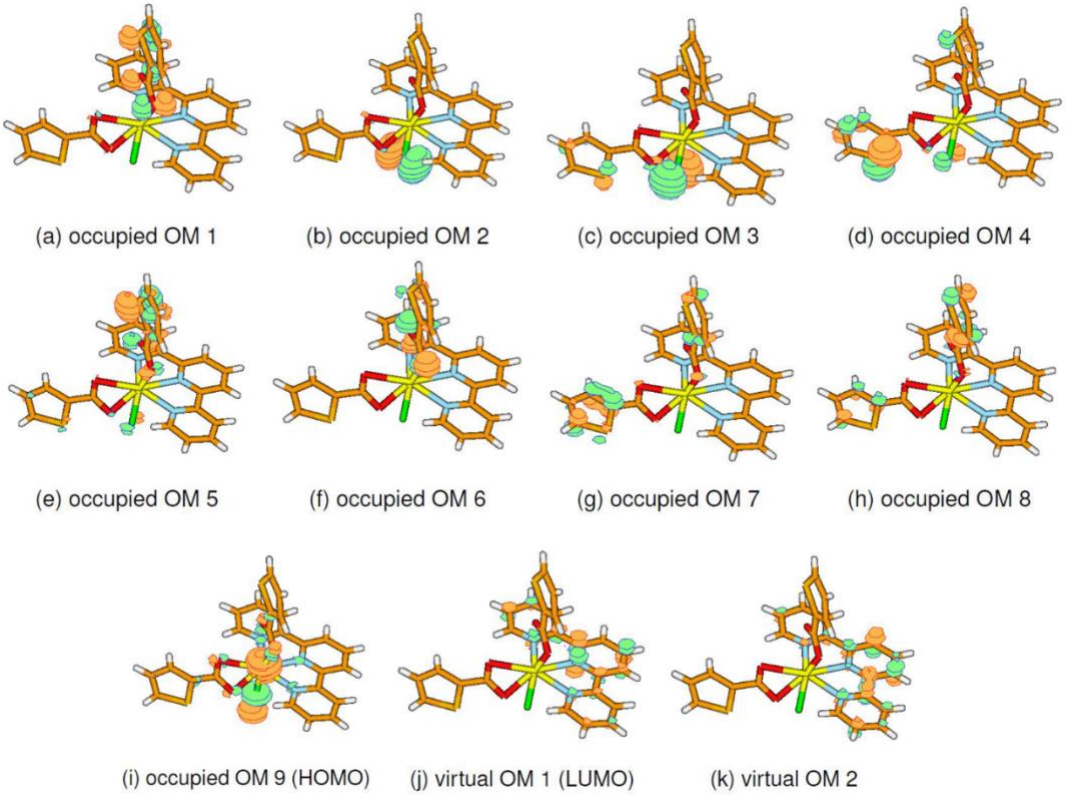

Figure S51. Calculated molecular orbital diagram for relevant **3A-Cl(a)** energy states involved transitions between 315-650 nm.

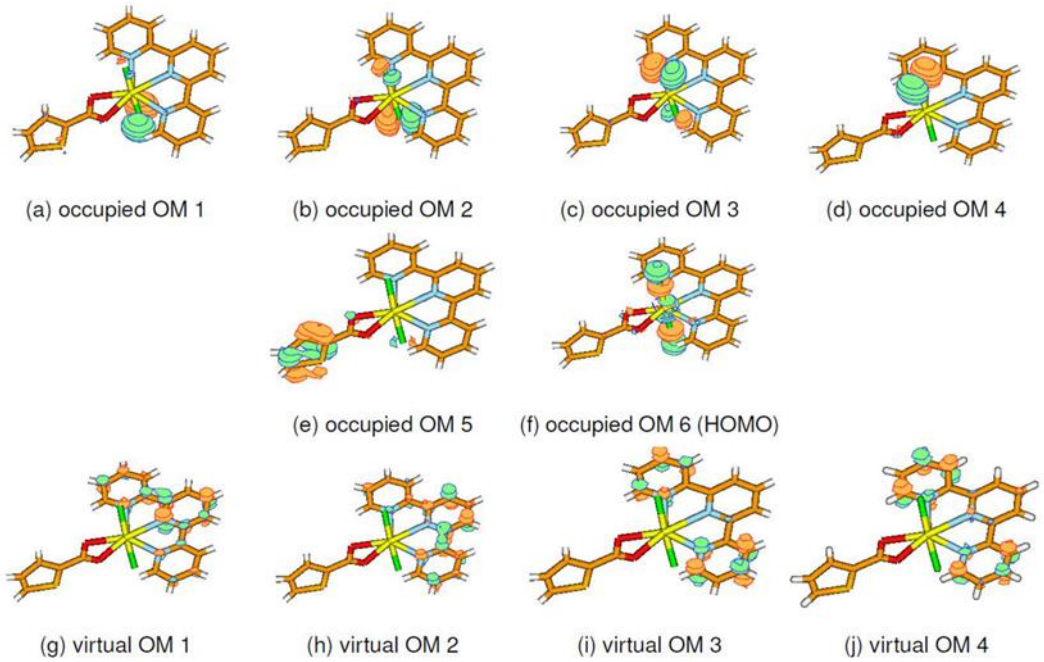

Figure S52. Calculated molecular orbital diagram for relevant **3A-Cl(c)** energy states involved transitions between 315-650 nm.

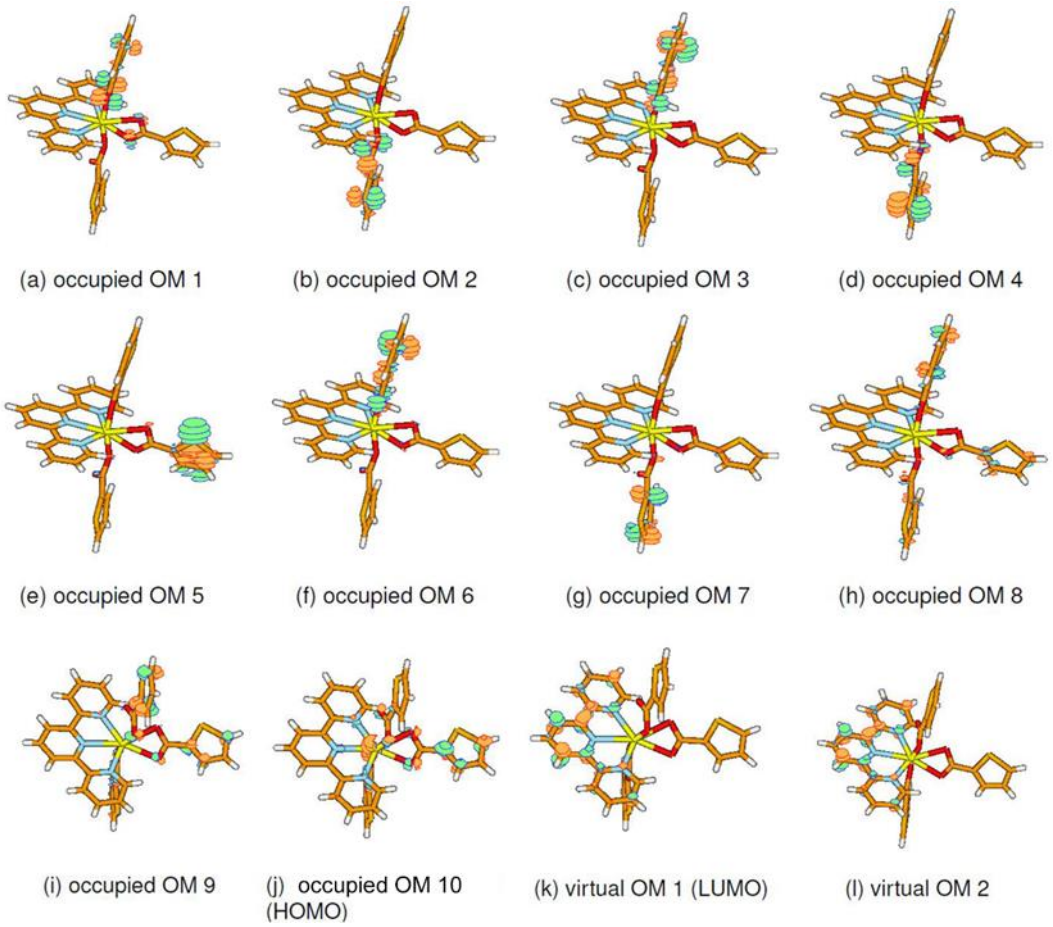

Figure S53. Calculated molecular orbital diagram for relevant **3A-Cl(c)** energy states involved transitions between 315-650 nm.

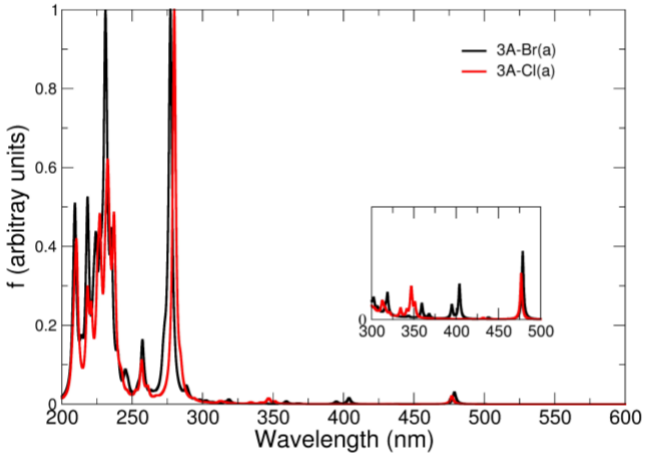

Figure S54. Comparison of calculated absorbance spectra for isomorphous **3A-Cl(a)** and **3A-Br(a)** monomers, whose structures/models are identical with exception of halide identity.

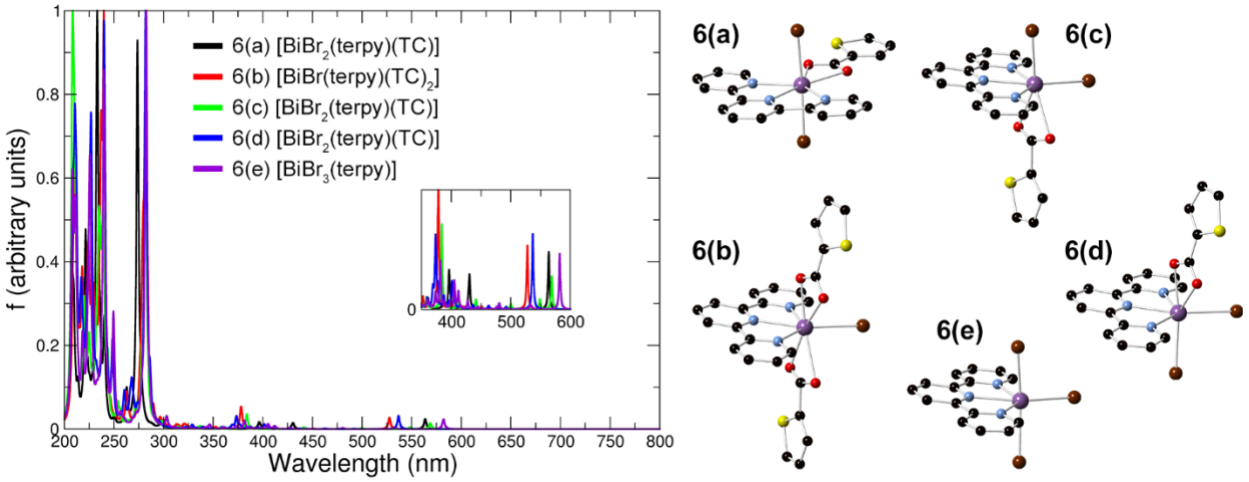

Figure S55. Calculated absorbance spectra of modeled monomeric cutouts derived from compound **6** with corresponding general formulas. Although **6(c**) and **6(d)** are isostructural, the Bi-Br bond distance for Br's trans to the TC unit appreciably vary, 2.8144(2) and 2.9757(2) Å respectively. Furthermore, not only does the lowest energy transition extend further into the visible with increased halide substituents as seen for other models reported herein, but also these transitions appear to blue shift with increasing Bi-X bond distance for isostructural units (e.g. **6(c)** and **6(d)**). This observed trend is also reflected in isostructural units **3A-Cl(a)** and **3B-Cl**. Likely influence of Bi lone pair stereochemical activity.

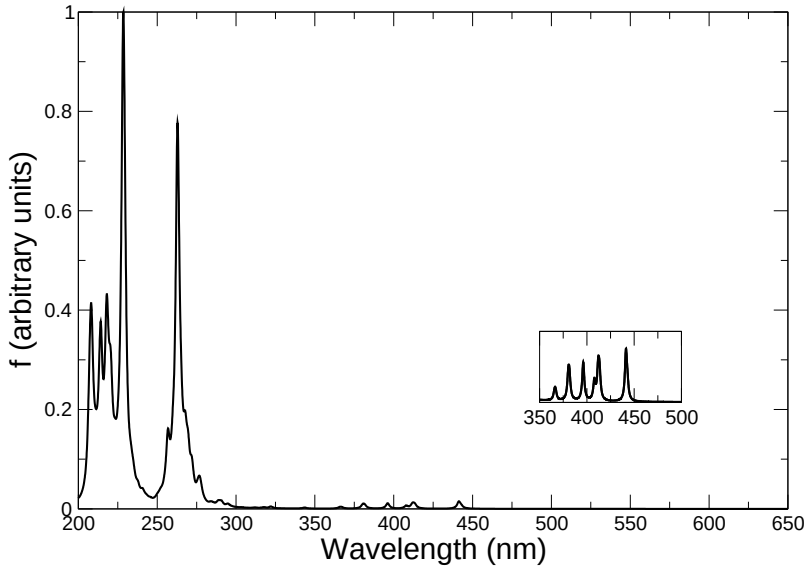

Figure S56. Calculated absorbance spectra from tructural cut-outs, derived from the single crystal structural data for compound **2.**

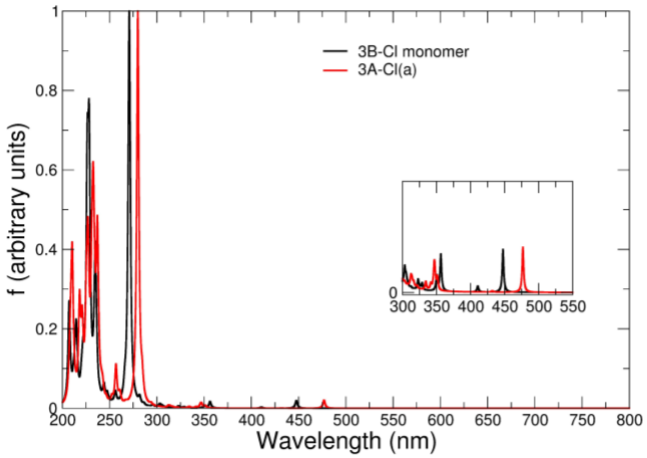

Figure S57. Comparison of calculated absorbance spectra for isostructural **3A-Cl(a)** and **3B-Cl** monomers.

References

1. Adcock, A. K.; Ayscue, R. L.; Breuer, L. M.; Verwiel, C. P.; Marwitz, A. C.; Bertke, J. A.; Vallet, V.; Réal, F.; Knope, K. E., Synthesis and photoluminescence of three bismuth(iii)-organic compounds bearing heterocyclic N-donor ligands. *Dalton Transactions* **2020,** *49* (33), 11756-11771.
2. Batrice, R. J.; Ridenour, J. A.; Ayscue, R. L.; Bertke, J. A.; Knope, K. E., Synthesis, structure, and photoluminescent behaviour of molecular lanthanide-2-thiophenecarboxylate-2,2 ':6 ',2 "-terpyridine materials. *Crystengcomm* **2017,** *19* (35), 5300-5312.
3. APEX3, SADABS, SAINT, SHELXTL, XCIF, XPREP. *Bruker AXS Inc.* **2016,** *Madison, WI, USA*.
4. Sheldrick, G., Crystal structure refinement with SHELXL. *Acta Crystallographica Section C* **2015,** *71* (1), 3-8.
5. Hubschle, C. B.; Sheldrick, G. M.; Dittrich, B., ShelXle: a Qt graphical user interface for SHELXL. *Journal of Applied Crystallography* **2011,** *44* (6), 1281-1284.
6. Spek, A., Single-crystal structure validation with the program PLATON. *Journal of Applied Crystallography* **2003,** *36* (1), 7-13.
7. Batrice, R. J.; Ayscue, R. L.; Adcock, A. K.; Sullivan, B. R.; Han, S. Y.; Piccoli, P. M.; Bertke, J. A.; Knope, K. E., Photoluminescence of Visible and NIR-Emitting Lanthanide-Doped Bismuth-Organic Materials. *Chemistry-a European Journal* **2018,** *24* (21), 5630-5636.